The Astrophysical Journal, 834:35 (19pp), 2017 January 1 doi:10.3847/1538-4357/834/1/35

THE NANOGRAV NINE-YEAR DATA SET: EXCESS NOISE IN MILLISECOND PULSAR ARRIVAL TIMES

M. T. Lam[1,2,3], J. M. Cordes[3], S. Chatterjee[3], Z. Arzoumanian[4], K. Crowter[5], P. B. Demorest[6], T. Dolch[7], J. A Ellis[8,21], R. D. Ferdman[9,10], E. Fonseca[5], M. E. Gonzalez[5,11], G. Jones[12], M. L. Jones[1,2], L. Levin[13], D. R. Madison[14], M. A. McLaughlin[1,2], D. J. Nice[15], T. T. Pennucci[1,2,12], S. M. Ransom[14], R. M. Shannon[16,17], X. Siemens[18], I. H. Stairs[5], K. Stovall[6,19], J. K. Swiggum[18], and W. W. Zhu[20]

[1] Department of Physics, West Virginia University, White Hall, Morgantown, WV 26506, USA; michael.lam@mail.wvu.edu
[2] Center for Gravitational Waves and Cosmology, West Virginia University, White Hall, Morgantown, WV 26506, USA
[3] Department of Astronomy and Cornell Center for Astrophysics and Planetary Science, Cornell University, Ithaca, NY 14853, USA
[4] Center for Research and Exploration in Space Science and Technology and X-Ray Astrophysics Laboratory, NASA Goddard Space Flight Center, Code 662, Greenbelt, MD 20771, USA
[5] Department of Physics and Astronomy, University of British Columbia, 6224 Agricultural Road, Vancouver, BC V6T 1Z1, Canada
[6] National Radio Astronomy Observatory, P.O. Box 0, Socorro, NM, 87801, USA
[7] Department of Physics, Hillsdale College, 33 E. College Street, Hillsdale, MI 49242, USA
[8] Jet Propulsion Laboratory, California Institute of Technology, 4800 Oak Grove Drive, Pasadena CA, 91109, USA
[9] Department of Physics, McGill University, 3600 rue Universite, Montreal, QC H3A 2T8, Canada
[10] Department of Physics, University of East Anglia, Norwich NR4 7TJ, UK
[11] Department of Nuclear Medicine, Vancouver Coastal Health Authority, Vancouver, BC V5Z 1M9, Canada
[12] Department of Physics, Columbia University, 550 W. 120th Street, New York, NY 10027, USA
[13] Jodrell Bank Centre for Astrophysics, School of Physics and Astronomy, The University of Manchester, Manchester M13 9PL, UK
[14] National Radio Astronomy Observatory, 520 Edgemont Road, Charlottesville, VA 22903, USA
[15] Department of Physics, Lafayette College, Easton, PA 18042, USA
[16] CSIRO Astronomy and Space Science, Australia Telescope National Facility, Box 76, Epping NSW 1710, Australia
[17] International Centre for Radio Astronomy Research, Curtin University, Bentley WA 6102, Australia
[18] Center for Gravitation, Cosmology and Astrophysics, Department of Physics, University of Wisconsin-Milwaukee, P.O. Box 413, Milwaukee, WI 53201, USA
[19] Department of Physics and Astronomy, University of New Mexico, Albuquerque, NM, 87131, USA
[20] Max-Planck-Institut für Radioastronomie, Auf dem Hügel 69, D-53121, Bonn, Germany
Received 2016 October 5; revised 2016 November 7; accepted 2016 November 9; published 2016 December 28

ABSTRACT

Gravitational wave (GW) astronomy using a pulsar timing array requires high-quality millisecond pulsars (MSPs), correctable interstellar propagation delays, and high-precision measurements of pulse times of arrival. Here we identify noise in timing residuals that exceeds that predicted for arrival time estimation for MSPs observed by the North American Nanohertz Observatory for Gravitational Waves. We characterize the excess noise using variance and structure function analyses. We find that 26 out of 37 pulsars show inconsistencies with a white-noise-only model based on the short timescale analysis of each pulsar, and we demonstrate that the excess noise has a red power spectrum for 15 pulsars. We also decompose the excess noise into chromatic (radio-frequency-dependent) and achromatic components. Associating the achromatic red-noise component with spin noise and including additional power-spectrum-based estimates from the literature, we estimate a scaling law in terms of spin parameters (frequency and frequency derivative) and data-span length and compare it to the scaling law of Shannon & Cordes. We briefly discuss our results in terms of detection of GWs at nanohertz frequencies.

Key words: gravitational waves – pulsars: general

1. INTRODUCTION

Recycled millisecond pulsars (MSPs) are the most stable astrophysical clocks in the universe (Verbiest et al. 2009). Such stability allows them to be used as tools in experiments of fundamental physics, including tests of gravitation (e.g., Zhu et al. 2015), constraints on general relativity (see Will 2014 for an overview), and detection of nanohertz to microhertz frequency gravitational waves (GWs; e.g., Arzoumanian et al. 2015a, 2016; Verbiest et al. 2016).

GWs will appear as temporally correlated stochastic deviations from a timing model that includes kinematic and astrometric terms that describe the pulsar–observatory line of sight (Sazhin 1978; Detweiler 1979; Hellings & Downs 1983; Romani 1989, p. 113; Foster & Backer 1990), as well as frequency-dependent pulse profile evolution and interstellar propagation effects (Craft 1970; Armstrong 1984; Blandford et al. 1984; Cordes & Shannon 2010; Foster & Cordes 1990; Rickett 1990). Detection of GWs is accomplished by measuring a specific, quadrupolar angular correlation in pulse time-of-arrival (TOA) deviations from many pulsars distributed over the sky (Hellings & Downs 1983). However, numerous other sources of noise, both temporally uncorrelated and correlated, contaminate our timing models and reduce each pulsar's contribution to the detection of GWs (e.g., Arzoumanian et al. 2015b; Lentati et al. 2016). Fortunately, many of these other sources are uncorrelated between pulsars, though errors in the reference time standard used, in the planetary ephemeris used, in polarization calibration, and more, can introduce spatial and therefore temporal correlations (van Straten 2013; Tiburzi et al. 2016).

Shannon & Cordes (2010, hereafter SC2010) investigated the strength and nonstationarity of long-term, correlated "red" noise in TOAs from pulsars in the literature. They attributed the red noise to rotational instabilities in individual pulsars, known as spin noise. Arguing that spin noise was the dominant source of red noise in the pulsars, they globally characterized and

[21] Einstein Fellow.

developed scaling relations of spin noise over all pulsar populations, finding that the spin noise was a steep-spectrum process ($\sim f^{-5}$) in a fit dominated by slow-period pulsars.

Other sources of red noise in TOAs are known. One such source is the interstellar medium (ISM), which causes radio-frequency-dependent delays in pulse arrival times (Lam et al. 2016b). The largest effect comes from a dispersive delay proportional to the dispersion measure (DM), the electron density integral along the line of sight, and the inverse radio frequency squared. The DM is typically estimated using multifrequency observations, and DM delays are removed by imposing some correlation structure in time (Keith et al. 2013; Arzoumanian et al. 2015b). Imperfect estimation of DM, from using incorrect temporal correlations, from the combination of asynchronously observed multifrequency data, or from frequency-dependent DMs due to interstellar scattering, will cause red noise in the timing residuals[22] (Lam et al. 2015, 2016b; Cordes et al. 2016). Other noise sources that can appear temporally correlated are possible, including variations in the pulse shape from interstellar scattering, polarization calibration (e.g., cross-coupling) errors, radio frequency interference (RFI), and pulsar mode changes (see Appendix A of Lam et al. 2016a, hereafter NG9WN).

The North American Nanohertz Observatory for Gravitational Waves (NANOGrav; McLaughlin 2013) collaboration observes a pulsar timing array for the detection and long-term study of GWs. The goal is to correlate arrival time differences in pulses from individual pulsars after a timing model and noise model have been accounted for, for each pulsar. Understanding the noise model is crucial for properly calibrating the array for optimal GW sensitivity (Lam et al. 2016a). This work aims to characterize the timing accuracy of the NANOGrav MSPs, paralleling the results of NG9WN to characterize their timing precision. Throughout this work, we will denote long-term (years) temporally correlated noise as "red noise" in reference to spectral power concentrated at low frequencies. We will denote changes of noise properties with radio observing frequency as "chromatic."

In Section 2, we describe the methodology for estimating the variance from stochastic noise processes. In Section 3, we describe the NANOGrav nine-year data set. We describe the implementation of the measured white-noise model for producing residuals and estimate the excess noise in our MSPs in Section 4; we discuss the pulsars individually in Section 5. In Section 6, we insert our measurements into the SC2010 data set and rederive the scaling relations for red noise in various pulsar class subsets. We summarize our conclusions in Section 7. For convenience, we provide a table of symbols used in the paper in Table 1.

2. VARIANCE OF STOCHASTIC PROCESSES WITH ADDITIVE NOISE

Our goal is to use pulsar timing residuals to determine the amount of excess variance over the white noise (WN) in our pulse arrival times. More generally, we want to measure the posterior probability density function (PDF) of the variance of stochastic processes when combined with some other independent processes, such as WN. In this section, we develop the formalism for measuring the variance of multiple processes in our timing residuals. For clarity, we will define $V_X \equiv \sigma_X^2$ to be

[22] Defined as TOAs minus timing model.

Table 1
Symbols and Acronyms Used

Symbols	Definition	Typical Units
A	Achromatic excess noise (AEN)	⋯
$A_{\rm r}$	Coefficient in power-law amplitude spectrum	μs yr$^{1/2}$
$B_{\rm chan}$	Channel bandwidth	MHz
C	Chromatic excess noise (CEN)	⋯
$\boldsymbol{C}$	Noise covariance matrix	μs^2
C_2	Spin noise fitting parameter for noise amplitude	⋯
DM	Dispersion measure	pc cm^{-3}
$D_{\overline{\mathcal{R}}}(\tau)$	Structure function of epoch-averaged residuals	μs^2
$\mathcal{F}$	Scaling factor on error (EFAC)	⋯
f	Fluctuation frequency	yr^{-1}
$f_{\rm D}$	Probability density function for detections	⋯
$f_{\rm UL}$	Probability density function for upper limits	⋯
$\Delta t_{{\rm FD},j}$	Frequency-dependent term in timing model	μs
i, j, k	Measurement indices	⋯
	For the variance analysis, i and j denote indices over time	⋯
	and frequency respectively.	⋯
	For the spin-noise analysis, i labels individual measurements,	⋯
	j labels detections of red noise, and k labels upper limits of red noise	⋯
$\mathcal{J}$	Error correlated in observing frequency (ECORR)	μs
$\mathcal{L}$	Likelihood or pseudolikelihood function	⋯
$n_{\rm ISS}$	Number of scintles	⋯
N	Number of measurements	⋯
$\mathcal{N}$	Normal distribution	⋯
$P(f)$	Power spectrum	μs^2 yr or yr^3
P_0	Amplitude of Reardon et al. (2016) power spectrum	yr^{-3}
$\mathcal{Q}$	Error added in quadrature (EQUAD)	μs
RP	Redness parameter, $D_{\overline{\mathcal{R}}}(\tau \geqslant 365\ {\rm days})/D_{\overline{\mathcal{R}}}(0 < \tau \leqslant 30\ {\rm days})$	⋯
$\mathcal{R}$	Timing residuals	μs
$\overline{\mathcal{R}}$	Epoch-averaged residuals	μs
s	Power-law index for chromatic noise	⋯
t	Observing time	Time
$T_{\rm obs}$	Total time span of single observation	min
T	Total time span of all observations	yr
$\mathcal{T}(f)$	Transmission function applied to power spectra	⋯
	to remove effects of timing model, normalized to unit height	⋯
V	Variance of a process or time series	μs^2
W	White noise (WN)	⋯
X	Generic process or time series	⋯
α	Spin-noise fitting parameter on spin frequency	⋯
$\alpha_{\rm r}$	Index of modified power-law power spectrum	⋯
	in Reardon et al. (2016)	⋯
β	Spin-noise fitting parameter on spin frequency derivative	⋯
γ	Spin-noise fitting parameter on total time span observed	⋯
$\gamma_{\rm r}$	Index of power-law power spectrum, $P(f) \propto f^{-\gamma_{\rm r}}$	⋯
δ	Spin-noise fitting parameter for noise scatter	⋯
$\delta_{XX'}$	Kronecker delta function	⋯
$\Delta t_{\rm d}$	Diffractive scintillation timescale	s
$\Delta \nu_{\rm d}$	Diffractive scintillation bandwidth	MHz
η	Dynamic spectrum filling factor	⋯
ν	Electromagnetic (radio) frequency	MHz
ν_0	Reference observing frequency	MHz
$\nu_{\rm band}$	Receiver band frequency	MHz
$\nu_{\rm s}$	Pulsar spin frequency	Hz

Table 1
(Continued)

Symbols	Definition	Typical Units
$\dot{\nu}_s$	Pulsar spin frequency derivative	Hz s^{-1}
σ	rms	μs
$\sigma_{\rm const}$	rms noise constant with pulse S/N,$\sigma_{\rm const} = \sqrt{\sigma_J^2 + \sigma_{\rm DISS}^2}$	μs
$\sigma_{\rm DISS}$	Diffractive interstellar scintillation error	μs
σ_J	Jitter error	μs
$\sigma_{S/N}$	Template-fitting error	μs
σ_r	Red noise error	μs
$\sigma_{TN,2}$	"Timing noise" after a quadratic fit, red noise measured in previous works	μs …
$\sigma_{\rm ex}$	Excess noise	μs
τ	Time lag	day
τ_d	Scattering timescale	μs

the variance of a process X_{ij} with rms σ_X, where i labels the measurement epoch and j labels the observed radio frequency. Through this section, our formalism will apply to generic processes with or without a temporal correlation structure; that is, we do not distinguish between excess red noise or excess WN.

2.1. Single Stochastic Process

Let the residuals $\mathcal{R}_{ij} = X_{ij} + W_{ij}$ be the measured process that is the sum of two Gaussian processes, where X_{ij} is the stochastic noise process of interest with the variance we wish to characterize, and W_{ij} is additive WN. We assume that both noise processes are zero mean; it therefore follows that $\mathcal{R}_{ij}$ will be zero mean.

Since $\mathcal{R}_{ij}$ is a zero-mean Gaussian process, the PDF of $\mathcal{R}_{ij}$ is simply a normal distribution $\mathcal{N}(0, V_{\mathcal{R}_{ij}})$, where $V_{\mathcal{R}_{ij}}$ represents the variance of $\mathcal{R}_{ij}$. We can separate each $V_{\mathcal{R}_{ij}}$ into the sum of the two variances $V_{X_{ij}} + V_{W_{ij}}$ since X_{ij} and W_{ij} are independent processes and the covariance between the two is zero. We define the total excess variance $V_{\rm ex}$ over the WN to be

$$V_{\rm ex} \equiv V_X = \langle X_{ij}^2 \rangle = \frac{1}{N} \sum_{i,j} X_{ij}^2, \tag{1}$$

where N is the number of measurements, and again X_{ij} is zero mean. The average denoted by angle brackets is taken over all indices i and j. Thus, for each measurement $\mathcal{R}_{ij}$ with WN measurement error $\sigma_{W_{ij}}$, we approximate the variance as $V_{\mathcal{R}_{ij}} = V_{\rm ex} + V_{W_{ij}}$. We define the pseudolikelihood function for $V_{\rm ex}$ as

$$\mathcal{L}(V_{\rm ex} | \{\mathcal{R}_{ij}, V_{W_{ij}}\}) \equiv \prod_{i,j} \frac{1}{\sqrt{2\pi (V_{\rm ex} + V_{W_{ij}})}} \exp\left[-\frac{\mathcal{R}_{ij}^2}{2(V_{\rm ex} + V_{W_{ij}})} \right]. \tag{2}$$

The width of the pseudolikelihood function (i.e., how well we can estimate $V_{\rm ex}$) will depend on the magnitude of the measurement errors $\sigma_{W_{ij}}$ and on the stationarity of $\sigma_{\rm ex}$. For example, any additional nonstationary noise processes, such as short-term (i.e., much less than the total data span) RFI, will increase not only the estimated $V_{\rm ex}$ but the error on $V_{\rm ex}$ as well.

The pseudolikelihood function is not strictly a likelihood function unless all $\mathcal{R}_{ij}$ in Equation (2) are independent, which is not known a priori. To test our pseudolikelihood function as a variance estimator, we simulated realizations of excess noise with power-law spectra between $P(f) \propto f^0$ and f^{-6} and added WN of varying strengths. We were able to recover the variance of the injected excess noise, suggesting that the derived $V_{\rm ex}$ is a good estimate of the true excess noise variance. We did not explore more complex noise processes, though our simulations indicate that correlations of various strengths will still yield the correct variance. Noise processes uncorrelated in time and frequency are independent and are therefore covered by a traditional likelihood function. For brevity, we will drop the "pseudo" in future discussion.

2.2. Achromatic and Chromatic Stochastic Processes

We now consider residuals $\mathcal{R}_{ij} = A_{ij} + C_{ij} + W_{ij}$ where A_{ij} and C_{ij} are two Gaussian processes. Again, W_{ij} is additive WN. We let $A_{ij} = A_i$ be a stochastic process that is achromatic (frequency-independent) and therefore only depends on time, such as rotational spin noise or GWs. We let C_{ij} be a process that is chromatic, such as from interstellar scattering corrections.

We must impose some frequency dependence on C_{ij}, otherwise we can place all of the variance from A_i into the time component of C_{ij}. Therefore, we define $C_{ij} \equiv C_i (\nu_j/\nu_0)^{-s}$, where C_i is the chromatic noise for epoch i, ν_0 is a reference frequency, and we select and fix the power-law index s (e.g., $s = 2$ for DM variations) in our analysis. As before, for a given measurement $\mathcal{R}_{ij}$ and the three independent processes, we can write the total variance as the sum of the three components, $V_{\mathcal{R}_{ij}} = V_{A_i} + V_{C_i} (\nu_j/\nu_0)^{-2s} + V_{W_{ij}}$, where the factor of 2 multiplying s comes from the expected value of C_{ij} squared. The (pseudo)likelihood function can now be written as

$$\mathcal{L}(V_A, V_C | \{\mathcal{R}_{ij}, \nu_j, V_{W_{ij}}\}, \nu_0, s) = \prod_{i,j} \frac{1}{\sqrt{2\pi (V_A + V_C (\nu_j/\nu_0)^{-2s} + V_{W_{ij}})}} \times \exp\left[-\frac{\mathcal{R}_{ij}^2}{2(V_A + V_C (\nu_j/\nu_0)^{-2s} + V_{W_{ij}})} \right], \tag{3}$$

where we have assumed that V_A and V_C represent the total of the achromatic and chromatic variances, respectively.

We convert estimates of the chromatic variance using one value of s to a new value of s' with

$$C_{ij} = C_i \left(\frac{\nu_j}{\nu_0} \right)^{-s} = C_i' \left(\frac{\nu_j}{\nu_0} \right)^{-s'}. \tag{4}$$

The variance of the process C_i' will then be

$$V_{C_i'} = V_{C_i} \left(\frac{\nu_j}{\nu_0} \right)^{-2(s-s')}. \tag{5}$$

When rescaling reference frequencies from ν_0 to ν_0'', the variance of the process C_i'' will be $V_{C_i''} = V_{C_i} (\nu_0''/\nu_0)^{-2s}$.

3. OBSERVATIONAL DATA: THE NANOGRAV NINE-YEAR DATA SET

Here we will briefly summarize our data. We used TOAs and parameter files from the NANOGrav nine-year data set described in Arzoumanian et al. (2015b, hereafter NG9) for our analysis. Observations of 37 MSPs were carried out at the Green Bank Telescope (GBT) and Arecibo Observatory (AO). We used two generations of back ends at each telescope, the GASP/GUPPI back ends at GBT and the ASP/PUPPI back - ends at AO (Demorest 2007; DuPlain et al. 2008; Ford et al. 2010; Demorest et al. 2013), with more recent back ends processing up to an order of magnitude larger bandwidth for improved pulse sensitivity. Observations of each pulsar at each epoch were made using two telescope receivers at widely separate frequencies.

Pulse profiles were folded and de-dispersed using an initial timing model with sufficient accuracy to keep any timing noise from profile shape changes at negligible levels (NG9WN). Polarization calibration and RFI excision algorithms were applied to the raw data profiles using the PSRCHIVE[23] software package (Hotan et al. 2004; van Straten et al. 2012). Prior to every pulsar observation, a broadband noise source was introduced into the two polarization signal paths between the receiver and the back-end systems, which allowed for differential gain and phase calibration. We allowed for the possibility that the noise source power in the two hands of polarization was not constant with time, and we therefore observed a bright, unpolarized quasar once per month per telescope per receiver band to properly calibrate the noise source.

After calibration, known RFI signals were excised, followed by a filtering process that removed frequency channels in which the off-pulse variation in a 20-channel-wide frequency window was four times greater than the median variation value. Throughout the data-reduction process, profiles observed within a single epoch were averaged together in time to reduce the data volume at each stage. The final pulse profiles used to generated TOAs were fully time averaged with some frequency averaging (the amount dependent on bandwidth) to build pulse signal-to-noise ratio (S/N). The final frequency resolution was of order of a few megahertz per channel, sufficient so that timing errors from frequency-dependent pulse profile evolution were negligible within each frequency channel (Pennucci et al. 2014; NG9WN). See NG9 for more details on the data processing.

Summing the two orthogonal polarization pulse profiles produced the intensity profiles used for arrival-time estimation. TOAs were generated from the multifrequency pulse profiles using a single smoothed template waveform per pulsar per telescope per receiver band and a Fourier-domain estimation algorithm (Taylor 1992). Using the TOAs and an initial timing model as a starting point, we fit timing parameters describing the spin, astrometry, and environmental properties (e.g., binary) of each pulsar. We used the TEMPO[24] software package for all timing parameter estimation. Spin-down and astrometric parameters were fit for all pulsars, and Keplerian parameters were fit for all binary pulsars. Post-Keplerian parameters were fit if they were deemed significant according to an F-test.

On a given epoch, we observed each pulsar over at least two receiver bands to estimate the dispersive delay due to the changing DM. We included one $\Delta\mathrm{DM}_i$ parameter (DMX) per epoch, which described the DM difference for that epoch from some fixed reference DM.[25] In addition, between zero and five, but typically no more than two, frequency-dependent (FD) time-delay terms ($\Delta t_{\mathrm{FD},j}$) were fit, modeling the time-independent pulse profile evolution as polynomials in the logarithm of the observing frequency. The significance of the $\Delta t_{\mathrm{FD},j}$ parameters was also determined by use of an F-test.

Lastly, in NG9 we used a parameterized noise model that included both white and red noise terms correlated differently in time and frequency (Arzoumanian et al. 2015a, 2016; NG9). Both Lam et al. (2016a) and our work take a different approach to NG9, but a comparison is made in the next section. The noise covariance matrix used in NG9 is

$$\boldsymbol{C}_{\nu\nu',tt'} = \delta_{tt'}\left[\delta_{\nu\nu'}\left(\mathcal{F}^2\sigma_{\mathrm{S/N}}^2 + \mathcal{Q}^2\right) + \mathcal{J}^2\right] + \boldsymbol{C}_{\mathrm{r}}(A_{\mathrm{r}}, \gamma_{\mathrm{r}}). \quad (6)$$

For TOAs with an associated error $\sigma_{\mathrm{S/N}}$ from template fitting, NG9 increased them with a scaling factor $\mathcal{F}$ (EFAC, $\approx$1 for all pulsars, to within a factor of 2 for most) and added additional variances in quadrature, one that characterized the correlations between receiver bands due to processes such as pulse jitter or RFI ($\mathcal{J}$, ECORR), and one that characterized additional additive noise ($\mathcal{Q}$, EQUAD). Finally, in NG9 we modeled red noise correlated in time ($\boldsymbol{C}_{\mathrm{r}}$) as a Gaussian process with a power-law spectrum

$$P(f) = A_{\mathrm{r}}^2\left(\frac{f}{1\ \mathrm{yr}^{-1}}\right)^{-\gamma_{\mathrm{r}}}, \quad (7)$$

where the spectral index γ_{r} is positive[26] for red noise, and A_{r} is the amplitude of the red noise in units of $\mu\mathrm{s\ yr}^{1/2}$. The normalization of $P(f)$ is such that the integral from $f = 0$ to $f = \infty$ gives the noise variance. The noise parameters were estimated with a Bayesian inference package[27] and fit for a joint likelihood with the timing model parameters. The uncertainties on the two red-noise parameters are often sizable with large covariances between the values. Both parameter (par) and TOA (tim) files from the NG9 data release are available at https://data.nanograv.org.

4. EXCESS NOISE ESTIMATION

Our goal is to estimate the amount of "postfit" excess noise in our timing residuals beyond the WN model described in NG9WN. We adjusted the TOA uncertainties and timing models used in NG9 in order to generate timing residuals for each pulsar. We can characterize the excess noise using those residuals.

[23] http://psrchive.sourceforge.net, accessed via scripts available at https://github.com/demorest/nanopipe.
[24] http://tempo.sourceforge.net
[25] Since different receiver bands are observed on different days in some cases, the DMX method assigns all TOAs within a given window of time to the same epoch, and then one $\Delta\mathrm{DM}_i$ is fit over that epoch. In the case of NG9, the window is typically 14 days.
[26] NG9 write the spectrum in the form $P(f) \propto f^{\gamma_{\mathrm{r}}}$ and list all of the values of γ_{r} as negative for red noise. In this work we will follow the common choice of γ_{r} being positive for red noise.
[27] https://github.com/jellis18/PAL2

4.1. The Reformulated Timing Model

We removed three pulsars from our analysis where WN parameters could not be estimated for at least one pulsar/back-end combination due to low pulse S/N. Otherwise, we added the jitter (σ_J) and diffractive interstellar scintillation (σ_{DISS}) errors from Table 3 of NG9WN in quadrature to the template-fitting errors ($\sigma_{S/N}$) after scaling them appropriately with time, such that the total TOA uncertainty becomes

$$\sigma_{S/N} \rightarrow [\sigma^2_{S/N} + \sigma^2_J(\nu_{band}, T_{obs}) + \sigma^2_{DISS}(\nu_{band}, B_{chan}, T_{obs})]^{1/2}, \quad (8)$$

where ν_{band} is the receiver band (not the frequency channel) of an individual observation, T_{obs} is the total time span of an individual observation, and B_{chan} is the channel bandwidth from which each TOA was generated (much less than the total of the observing band). We explicitly specify ν_{band} because WN parameters are a function of observing band in NG9WN. The jitter noise σ_J is proportional to $T_{obs}^{-1/2}$ and is independent of observing bandwidth over our receiver bandwidth ranges (see Shannon et al. 2014 for evidence of jitter decorrelation over $\sim$2 GHz for PSR J0437−4715). The scintillation noise non-trivially scales with bandwidth and time according to the formula

$$\sigma_{DISS} \approx \frac{\tau_d}{\sqrt{n_{ISS}}} \approx \tau_d \left[\left(1 + \eta_t \frac{T_{obs}}{\Delta t_d}\right)\left(1 + \eta_\nu \frac{B_{chan}}{\Delta \nu_d}\right)\right]^{-1/2}, \quad (9)$$

where $\tau_d \propto \nu^{-4.4}$ is the scattering timescale, n_{ISS} is the number of scintles, and $\Delta t_d \propto \nu^{1.2}$ and $\Delta \nu_d \propto \nu^{4.4}$ are the scintillation bandwidth and timescale, respectively. Proportionalities with radio frequency are given for a Kolmogorov medium (Cordes & Rickett 1998; Cordes & Lazio 2002). The filling factors η_t, η_ν are typically in the range 0.1 to 0.3 (Cordes & Shannon 2010; Levin et al. 2016); we chose them to be 0.2 as in NG9WN. Jitter and scintillation noise were scaled in NG9WN to 30 minute observation durations and bandwidths equal to that of the full band (rather than the channel bandwidth), as provided in NG9. Each TOA in NG9 was derived from data with duration 20−30 minutes and with channel bandwidths between 1.6 and 12.5 MHz depending on the telescope receiver; we make sure to scale the errors appropriately for every individual TOA. For pulsars with upper limits on σ_J, we set the value of σ_J we use equal to its 95% upper limit, providing us with conservative lower bounds on the excess noise.

For convenience, we define the rms noise that is constant with (independent of) pulse S/N:

$$\sigma_{const} = \sqrt{\sigma_J^2 + \sigma_{DISS}^2}, \quad (10)$$

which we will define with the subscript "const" to avoid confusion with the rms of the chromatic excess noise σ_C. For many pulsar/back-end combinations, NG9WN were able to use σ_{const} along with scintillation-estimated measurements of σ_{DISS} in order to estimate σ_J. For a few pulsar/back-end combinations, that was not the case (given the time and frequency resolution of their analysis), and those pulsars will be highlighted later in Section 5.

After we constructed our new TOA errors, we used the TEMPO2 software package accessed via libstempo[28] to refit the timing model (Hobbs et al. 2006). We used the same set of timing parameters as used in NG9, but we refit them after removing the noise model. We used the resulting postfit residuals (i.e., measured TOAs minus model TOAs) to generate the noise estimates made throughout the present work. We note that inclusion or exclusion of individual timing model parameters could bias our results. However, unless the excess noise follows the exact signature of timing delays of a timing model parameter, the inclusion of new parameters, such as additional post-Keplerian binary terms, will not reduce the excess noise variance substantially. Parameters included in the fit will always reduce the variance, but if the parameter is of low significance, then the evidence for the delays containing that signature is low and the excess noise will be minimally affected.

Since TEMPO and TEMPO2 minimize the χ^2 of the overall timing fit, in some cases they find the minimum by separating TOAs from different receiver bands within a given epoch, producing different sets of residuals as a function of receiver band that do not track each other. The splitting of residuals results from power preferentially being absorbed by the achromatic spin, astrometric, and orbital terms. In other words, there is covariance between the achromatic and chromatic timing parameters. We do not believe these solutions to be physical, and therefore we decided to iteratively solve for the best-fit timing solution, facilitated by our use of libstempo.

Starting with the NG9 timing parameter values, we fixed trial values of ΔDM_i and $\Delta t_{FD,j}$, refit the achromatic parameters and generated residuals with libstempo, and then determined a new set of fixed trial chromatic parameters using a least-squares method that minimized the "intraepoch" variance, defined as follows. For all epochs defined by the DMX time bins from NG9, we calculated the epoch-averaged residuals $\overline{\boldsymbol{\mathcal{R}}}$ (in matrix form) from the raw residuals $\boldsymbol{\mathcal{R}}$ by following the procedure in Arzoumanian et al. (2015a):

$$\overline{\boldsymbol{\mathcal{R}}} = (\boldsymbol{U}^T \boldsymbol{C}^{-1} \boldsymbol{U})^{-1} \boldsymbol{U}^T \boldsymbol{C}^{-1} \boldsymbol{\mathcal{R}}. \quad (11)$$

Here, $\boldsymbol{U}$ is the "exploder" matrix that maps the epochs to the full set of TOAs (see also Arzoumanian et al. 2014), and the noise covariance matrix can be written as

$$\boldsymbol{C}_{\nu\nu',tt'} = \delta_{tt'}[\delta_{\nu\nu'}\sigma^2_{S/N}(S) + \sigma^2_J(\nu_{band}, T_{obs})] + \rho_{DISS,\nu\nu',tt'}\sigma^2_{DISS}(\nu_{band}, B_{chan}, T_{obs}), \quad (12)$$

following the form in NG9WN, where ρ_{DISS} encapsulates the frequency and time correlation scales for DISS. The intraepoch variance is then simply

$$\sum_i (\mathcal{R}_{ij} - \overline{\mathcal{R}}_i)^2. \quad (13)$$

Note that in practice there can be multiple observations at the same frequency spaced by several days within any given epoch, but we subtract a single value from all of the residuals in that time range. Our procedure serves to keep infinite-frequency residuals from the same epoch close in pulse phase while allowing for TEMPO2 to find the best-fit achromatic

[28] https://github.com/vallis/libstempo

Table 2
Components Included in Three Noise Models for Timing Fit

Model	$\sigma_{S/N}$	$\mathcal{F}$	$\mathcal{Q}$	$\mathcal{J}$	A_r, γ_r	σ_J	σ_{DISS}	Fitting Method
A	×	×	×	×	×			TEMPO
B	×	…	…	…	…	…	…	Iterative TEMPO2 via libstempo
C	×	…	…	…	…	×	×	Iterative TEMPO2 via libstempo

Note. Columns are as follows: model label, template-fitting error ($\sigma_{S/N}$), TOA error scaling factor (EFAC, $\mathcal{F}$), TOA additive error (EQUAD, $\mathcal{Q}$), TOA frequency-correlated error (ECORR, $\mathcal{J}$), power-law red-noise parameters (A_r, γ_r), jitter error (σ_J), diffractive interstellar scintillation error (σ_{DISS}), and fitting method.

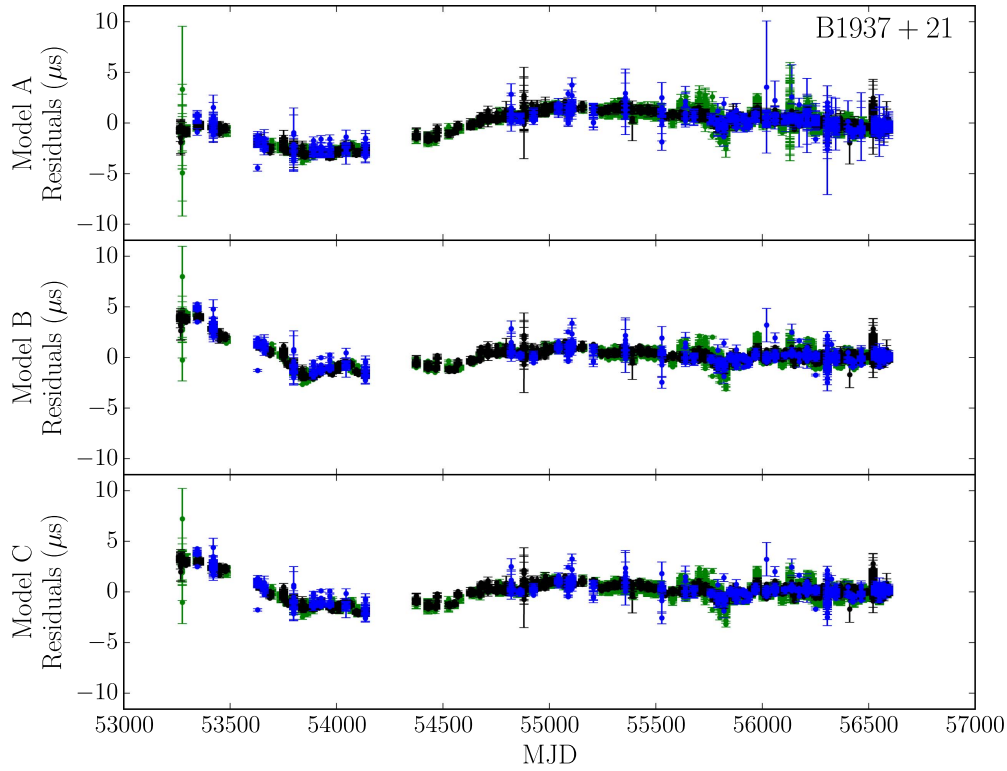

Figure 1. Comparison of residuals using the different noise models defined in Table 2. Error bars show the full white-noise TOA uncertainties. Colors indicate different observing bands: 820 MHz (green), 1400 MHz (black), and 2300 MHz (blue).

timing parameters. We found that the ΔDM_i parameters typically differed by $\lesssim 1\sigma$ from the NG9 values except for a few epochs across all pulsars. The $\Delta t_{FD,j}$ parameters typically differed by $\ll 1\sigma$.

Table 2 provides a summary of three different possible noise models for the timing fit. Model A comes directly from NG9. Model B removes all additional noise parameters except for the template-fitting errors on the TOAs; we show it for comparison purposes only. Again, in order to achieve a phase-connected solution between receiver bands, we use our iterative timing model approach discussed previously. Model C starts with the model B TOAs and adds in the appropriately scaled jitter and scintillation noise parameters from NG9WN. It is model C we test throughout this work.

We show a comparison of the timing residuals for PSR B1937+21 obtained from the three noise models in Figure 1. PSR B1937+21 has the smallest template-fitting and jitter errors in NG9 within each given receiver band both at AO and GBT (NG9WN), while its scintillation noise is the largest of the three WN terms, which is atypical for pulsars in our data set. We show its residuals as an example to demonstrate the effect of the timing model refit because it is not dominated by template-fitting errors and has known red noise residuals (e.g., Shannon & Cordes 2010; Arzoumanian et al. 2015b; Lentati et al. 2016). As expected visually from Figure 1, we see that PSR B1937+21 contains excess noise beyond the WN model.

Throughout this section, we report detections on the rms excess noise with the median value from the PDFs and the ±34.1% errors. Since we perform our likelihood calculations in the logarithm of variance and convert the PDFs to linear rms, we see tails in the distribution of log-variance toward smaller values ($V \to 0$) that become narrow peaks of probability in linear-rms space at $\sigma \approx 0$. Choosing the median value is robust against biasing our results to zero. We find that the median values are within the errors of the maximum likelihood values in log-variance. Detections must be "2σ" significant, otherwise we report the nondetection values as 95% upper limits. The results for our two variance analyses will be reported farther down in Table 3.

Table 3
Summary of Excess Noise Parameters

Pulsar	Obs	DM (pc cm^{-3})	T (yr)	σ_{ex} (μs)	σ_A (μs)	σ_C at 1 GHz (μs)	σ_W (μs)	RP	V_r/V_{tot}
J0023+0923[a]	AO	14.3	2.3	$0.31^{+0.05}_{-0.04}$	$0.30^{+0.04}_{-0.05}$	<0.02	5.35 ± 0.08	0.5 ± 0.2	−1.04 ± 0.87
J0030+0451	AO	4.3	8.8	$0.68^{+0.05}_{-0.04}$	0.67 ± 0.05	<0.06	3.22 ± 0.08	9.0 ± 2.5	0.89 ± 0.03
J0340+4130[a]	GBT	49.6	1.7	1.1 ± 0.2	<1.16	<0.98	6.87 ± 0.06	1.9 ± 0.7	0.48 ± 0.20
J0613−0200[a]	GBT	38.8	8.6	0.54 ± 0.02	$0.53^{+0.02}_{-0.03}$	<0.17	2.45 ± 0.04	9.3 ± 2.4	0.89 ± 0.03
J0645+5158[a]	GBT	18.2	2.4	$0.10^{+0.02}_{-0.01}$	<0.11	<0.08	3.47 ± 0.04	0.6 ± 0.2	−0.64 ± 0.67
J0931−1902[a]	GBT	41.5	0.6	<0.76	<0.39	<0.50	7.80 ± 0.21	…	…
J1012+5307[a]	GBT	9.0	9.2	1.91 ± 0.03	1.33 ± 0.06	1.26 ± 0.06	6.76 ± 0.08	1.4 ± 0.2	0.28 ± 0.12
J1024−0719[a]	GBT	6.5	4.0	$0.33^{+0.05}_{-0.04}$	$0.30^{+0.06}_{-0.07}$	<0.18	5.90 ± 0.07	1.5 ± 0.3	0.34 ± 0.14
J1455−3330[a]	GBT	13.6	9.2	$0.6^{+0.2}_{-0.1}$	<0.67	<0.38	9.47 ± 0.11	1.8 ± 0.4	0.43 ± 0.14
J1600−3053[a,b]	GBT	52.3	6.0	$0.19^{+0.04}_{-0.03}$	<0.06	0.61 ± 0.03	1.67 ± 0.01	1.7 ± 0.3	0.42 ± 0.11
J1614−2230[a]	GBT	34.5	5.1	<0.21	<0.15	<0.19	2.66 ± 0.02	4.0 ± 1.6	0.75 ± 0.10
J1640+2224[a,b]	AO	18.5	8.9	0.40 ± 0.02	<0.18	0.085 ± 0.005	3.18 ± 0.07	2.6 ± 0.7	0.61 ± 0.10
J1643−1224[a,b]	GBT	62.4	9.0	$2.36^{+0.04}_{-0.03}$	1.92 ± 0.06	1.21 ± 0.07	2.28 ± 0.02	2.2 ± 0.7	0.55 ± 0.14
J1713+0747	AO+GBT	16.0	8.8	0.123 ± 0.003	$0.119^{+0.004}_{-0.005}$	<0.10	2.36 ± 0.04	1.0 ± 0.2	−0.01 ± 0.16
	AO	…	8.8	$0.116^{+0.004}_{-0.003}$	0.115 ± 0.004	<0.05	1.23 ± 0.04	…	…
	GBT	…	7.7	$0.123^{+0.007}_{-0.006}$	0.132 ± 0.009	$0.09^{+0.02}_{-0.04}$	2.72 ± 0.04	…	…
J1738+0333[a]	AO	33.8	4.0	<0.21	<0.13	<0.36	4.87 ± 0.07	1.0 ± 0.9	−0.04 ± 1.01
J1741+1351[a]	AO	24.2	4.2	<0.12	<0.10	<0.05	2.29 ± 0.05	0.4 ± 0.1	−1.78 ± 1.16
J1744−1134	GBT	3.1	9.2	0.39 ± 0.01	0.39 ± 0.01	<0.04	2.55 ± 0.03	0.7 ± 0.2	−0.37 ± 0.34
J1853+1303[a]	AO	30.6	5.6	<0.25	<0.17	<0.10	3.87 ± 0.08	2.1 ± 0.7	0.53 ± 0.15
B1855+09[a]	AO	13.3	8.9	0.86 ± 0.02	0.85 ± 0.02	<0.05	2.57 ± 0.05	2.9 ± 1.5	0.65 ± 0.18
J1903+0327[a,b]	AO	297.6	4.0	$1.31^{+0.06}_{-0.07}$	<0.86	$3.2^{+0.2}_{-0.3}$	2.73 ± 0.05	4.3 ± 1.3	0.77 ± 0.07
J1909−3744	GBT	10.4	9.1	0.071 ± 0.004	<0.04	0.070 ± 0.004	1.08 ± 0.01	0.8 ± 0.1	−0.20 ± 0.22
J1910+1256	AO	38.1	8.8	1.49 ± 0.05	$1.46^{+0.06}_{-0.14}$	<1.88	2.92 ± 0.05	2.1 ± 0.5	0.51 ± 0.11
J1918−0642[a]	GBT	26.6	9.0	0.24 ± 0.05	<0.25	<0.26	5.73 ± 0.05	1.5 ± 0.3	0.34 ± 0.14
J1923+2515[a]	AO	18.9	1.6	$1.0^{+0.2}_{-0.1}$	0.9 ± 0.1	<0.09	5.11 ± 0.12	0.6 ± 0.3	−0.82 ± 0.86
B1937+21	AO+GBT	71.0	9.1	0.742 ± 0.006	0.741 ± 0.006	<0.07	0.21 ± 0.01	25.2 ± 5.9	0.960 ± 0.009
	AO	…	8.9	$0.703^{+0.011}_{-0.010}$	$0.702^{+0.011}_{-0.010}$	<0.10	0.18 ± 0.01	…	…
	GBT	…	9.1	0.756 ± 0.007	0.755 ± 0.007	<0.06	0.22 ± 0.01	…	…
J1944+0907	AO	24.3	5.7	$2.02^{+0.10}_{-0.09}$	$2.01^{+0.10}_{-0.09}$	<0.10	7.87 ± 0.24	2.5 ± 1.5	0.60 ± 0.24
B1953+29[a]	AO	104.5	7.2	1.7 ± 0.1	<0.83	0.66 ± 0.06	4.03 ± 0.08	1.3 ± 0.6	0.24 ± 0.34
J2010−1323[a]	GBT	22.2	4.1	$0.41^{+0.08}_{-0.07}$	<0.49	<0.28	4.27 ± 0.04	1.5 ± 0.5	0.34 ± 0.20
J2017+0603[a]	AO	23.9	1.7	<0.14	<0.10	<0.09	2.06 ± 0.05	0.4 ± 0.2	−1.38 ± 1.25
J2043+1711[a]	AO	20.7	2.3	<0.14	<0.10	<0.05	1.23 ± 0.03	0.5 ± 0.2	−0.96 ± 0.92
J2145−0750	GBT	9.0	9.1	0.75 ± 0.02	0.75 ± 0.02	<0.08	7.86 ± 0.13	1.0 ± 0.3	0.04 ± 0.26
J2214+3000	AO	22.6	2.1	$0.76^{+0.08}_{-0.07}$	0.75 ± 0.07	<0.34	5.86 ± 0.09	0.7 ± 0.2	−0.39 ± 0.48
J2302+4442[a]	GBT	13.7	1.7	<1.20	<0.83	<0.53	9.73 ± 0.11	0.5 ± 0.2	−1.08 ± 0.82
J2317+1439	AO	21.9	8.9	0.42 ± 0.02	0.41 ± 0.02	<0.02	2.62 ± 0.09	1.1 ± 0.5	0.10 ± 0.41

Notes. Columns are as follows: pulsar name, observatory, dispersion measure (DM), observed time span (T), single-process excess noise (σ_{ex}), achromatic excess noise (σ_A), chromatic excess noise (σ_C), white noise (σ_W), redness parameter (RP $= D_{\overline{\mathcal{R}}}(\tau \geqslant 365)/D_{\overline{\mathcal{R}}}(\tau \leqslant 30)$, excluding PSR J0931−1902 because $T \leqslant 1$ year), and the fraction of red noise variance (V_r/V_{tot}). For PSRs J1713+0747 and B1937+21, we show the variance analyses after the full timing model fit but separately considering residuals from the individual telescopes.

[a] Pulsars where there is an upper limit in the WN parameters for at least one frequency band.

[b] Pulsars where σ_{const} is smaller than the scintillation-estimated σ_{DISS}.

4.2. Single Stochastic Process

Using the model C residuals, we followed the methodology laid out in Section 2 for calculating the total excess noise. Figure 2 shows the results of the likelihood analysis for a single excess noise process (the measured excess beyond the WN) in the NANOGrav pulsars using the model C residuals. All values are shown unnormalized to the length of the data span; we expect longer data sets to show increased excess noise, either from the presence of red noise or potentially from increased probability of other noise sources (e.g., RFI) being introduced. The total time span observed for each pulsar is shown in parentheses.

PSRs J1909−3744 and J1713+0747 are two of the best-timed pulsars observed by NANOGrav, both high in S/N with very low WN (NG9WN). We note that they also show the lowest amounts of detected excess noise of all of the NANOGrav pulsars in our analysis. Many of the pulsars with the highest measured values are consistent with those that displayed significant red noise in NG9. Five of the top six detections (PSRs J1643−1224, J1944+0907, B1953+29, J1910+1256, and J1903+0327) were the pulsars in NG9 for which frequency-dependent timing residuals, induced by unmodeled ISM propagation effects, were claimed to be the dominant cause of the excess noise. Our next analysis is better suited for determining if such chromatic effects may be present

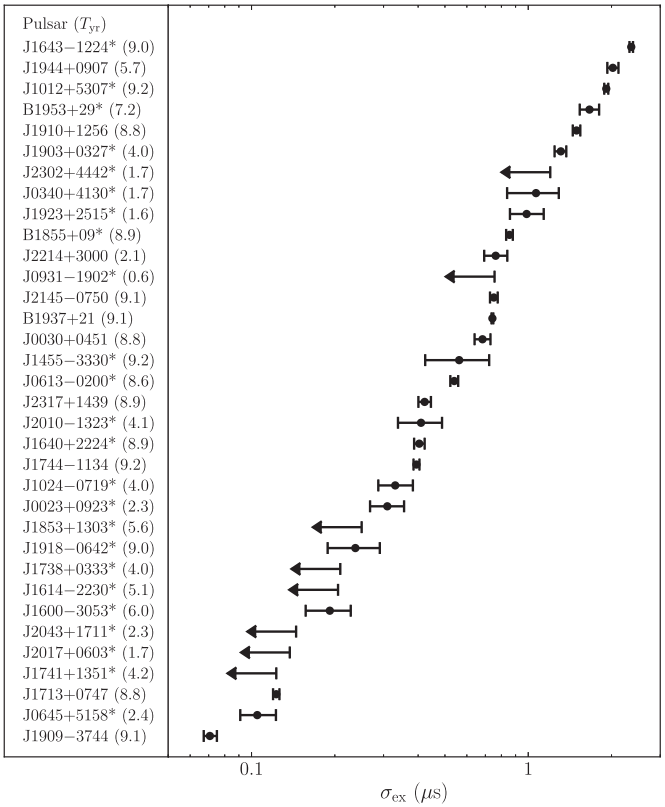

Figure 2. Measured excess noise for each of the NANOGrav pulsars ranked by decreasing value. The values in parentheses show the total time span observed for each pulsar, in years. Asterisks indicate pulsars for which the white-noise model is an upper limit (an upper limit in σ_{const}) for at least one receiver band. We report detections with the median likelihood value and the ±34.1% errors, with upper limits shown at the 95% level.

in the data. The third pulsar, PSR J1012+5307, also showed measurable red noise in NG9 though without frequency dependence.

4.3. Achromatic and Chromatic Stochastic Processes

Again using the model C residuals, we calculated the variance of an achromatic and a chromatic process in the timing residuals for each pulsar. For the chromatic component, we fixed $s = 2$ to account for effects such as imperfect DM estimation, and we define the reference frequency to be $\nu_0 = 1000$ MHz. We show the result of the analysis for PSR B1937+21 in Figure 3. The timing residuals are shown in the top right with the different receiver bands colored (820 MHz, green; 1400 MHz, black; 2300 MHz, blue). The two-dimensional likelihood surface $\mathcal{L}(V_A, V_C)$ is shown in the bottom left. The marginalized PDFs are shown above and to the right of the likelihood. For PSR B1937+21, we see a well-constrained measurement of achromatic excess noise (AEN) variance but an upper limit on the chromatic excess noise (CEN) variance, consistent with the fact that the timing residuals are correlated in time but the residuals track each other in frequency.

Figures 4–7 show the same likelihood analysis for four other pulsars. PSRs J1713+0747 and J1909−3744 are two of the best-timed pulsars in the NANOGrav pulsar timing array, each with detections of the variance of both noise processes. The analysis for PSR J1738+0333 is shown as an example of upper limits in both the achromatic and the chromatic excess noise. Lastly, we show the results for PSR J1910+1256 as it has a long stretch of single-frequency observations; therefore some chromatic DM variations may be best described by an achromatic noise process in our likelihood analysis. We discuss the problem in greater detail in the next section.

Figure 8 shows the results of our achromatic/chromatic likelihood analyses for all pulsars similar to Figure 2 in the case of a single excess noise process. Note that while we previously plotted the achromatic/chromatic likelihood PDFs in the logarithm of the variance, we calculated the median likelihood values, parameter errors, and upper limits using the marginalized PDFs of the rms achromatic/chromatic errors. In Figure 8, we order the pulsars by the AEN to rank by the known irreducible noise (which may not be true if our estimates of AEN are contaminated by chromatic processes, discussed later), whereas it is unclear if CEN can be corrected for in the future. We reemphasize that the noise values we report are unnormalized to the length of the total data span; we expect that pulsars observed for longer will in general show increased red, and therefore excess, noise. Again, the total time span observed is shown in parentheses for each pulsar.

In Figure 9, we include estimates of the WN,

$$V_W = \frac{1}{N}\sum_{i,j} W_{ij}^2, \tag{14}$$

for each pulsar to show the total noise budget for the NANOGrav pulsar timing array. We order the pulsars by their WN values. We note that the rms WN will contain varying contributions from residuals at each observing band, whose noise properties change as a function of receiver band. Changes in the length of each individual observation will also affect the TOA errors and therefore the measured WN. As a result, even one of our most precisely timed pulsars like PSR J1713+0747 can be ranked higher up in the plot. We emphasize that we are measuring the total sum of the WN in the nine-year data release, and that future predictions of white-noise performance should come from NG9WN.

Of the five pulsars in NG9 that were claimed to have red noise likely from ISM propagation effects, three show CEN in our analysis: PSRs J1643−1224, J1903+0327, and B1953+29. These three pulsars are three of the top four highest DM pulsars in NG9. In Figure 10, we explore the possible relationship between σ_C and ISM noise by plotting versus DM. Colors show which telescopes and receiver bands were used to observe each pulsar. While generally the CEN increases with DM, PSR J1012+5307 is an outlier. Frequency dependence between the two bands of residuals for PSR J1012+5307 is clear for several epochs upon visual inspection, but the cause, astrophysical or otherwise, is presently unknown.

Changing the power-law index s for the frequency dependence of the CEN may significantly alter our results. Interstellar scattering, for example, likely affects our observed pulsar signals with timing delays that will scale between approximately $s = 4$ and $s = 4.4$ depending on the scattering medium (e.g., Keith et al. 2013; Levin et al. 2016). Including a second term in the chromatic component of the likelihood function may be useful for distinguishing the relative strengths of both DM misestimation and scattering variation processes, both of which are likely to be present for high-DM pulsars. However, because of the large covariances between both power laws, our

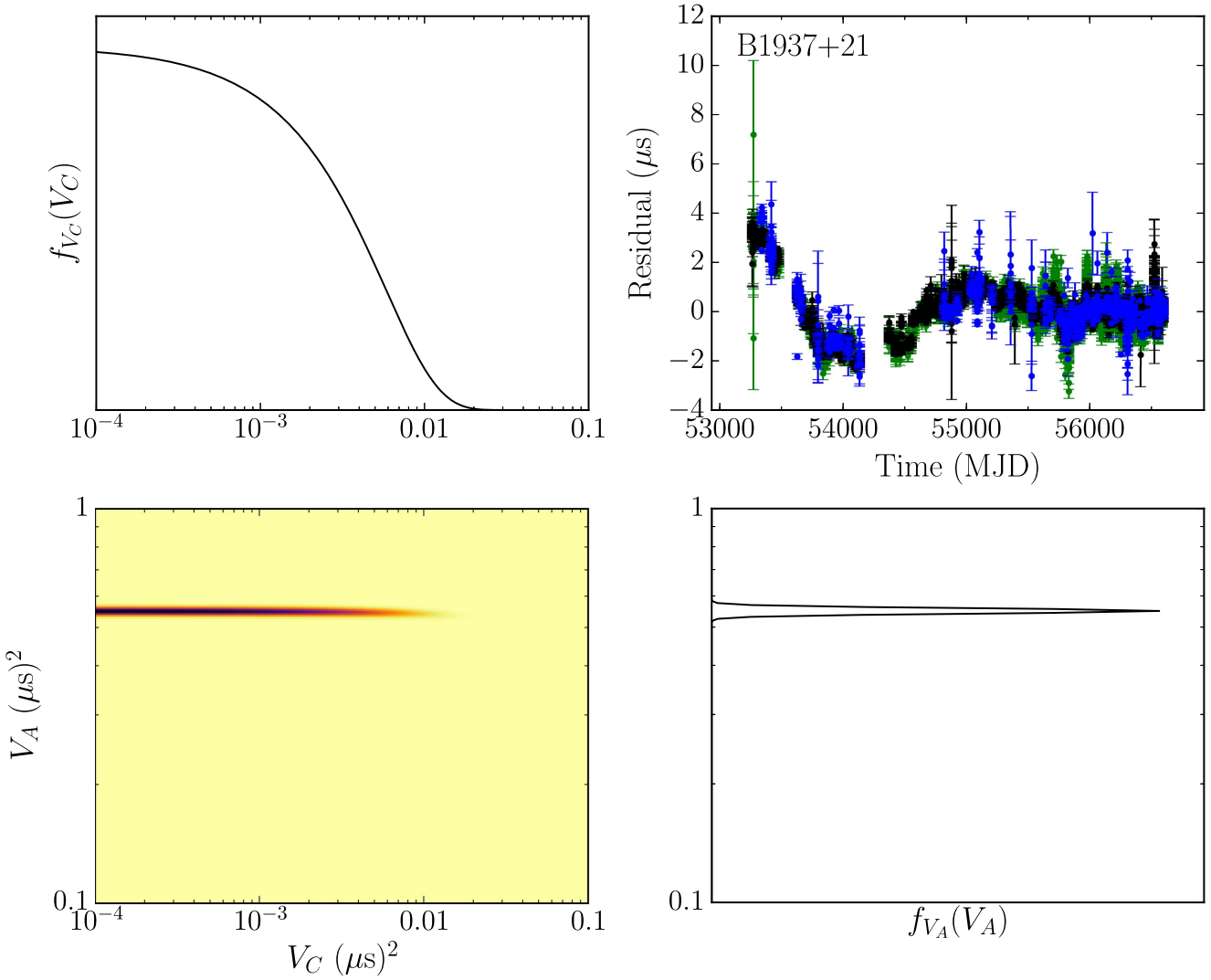

Figure 3. Achromatic/chromatic stochastic process likelihood analysis for PSR B1937+21. Bottom left: two-dimensional likelihood surface. The marginalized distributions are shown at the top and to the right. Top right: timing residuals (820 MHz, green; 1400 MHz, black; 2300 MHz, blue) for reference.

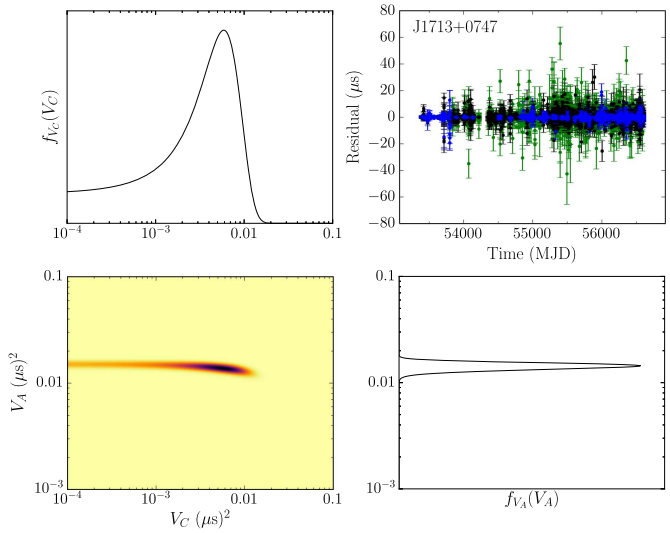

Figure 4. Achromatic/chromatic stochastic process likelihood analysis for PSR J1713+0747. See the caption to Figure 3 for more details.

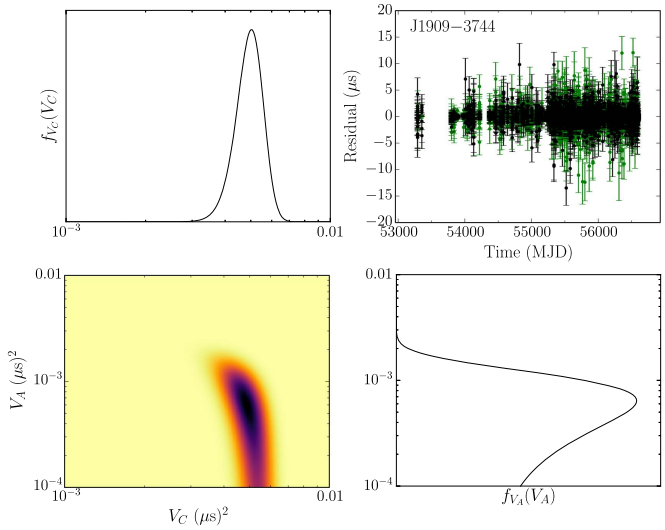

Figure 5. Achromatic/chromatic stochastic process likelihood analysis for PSR J1909−3744. See the caption to Figure 3 for more details.

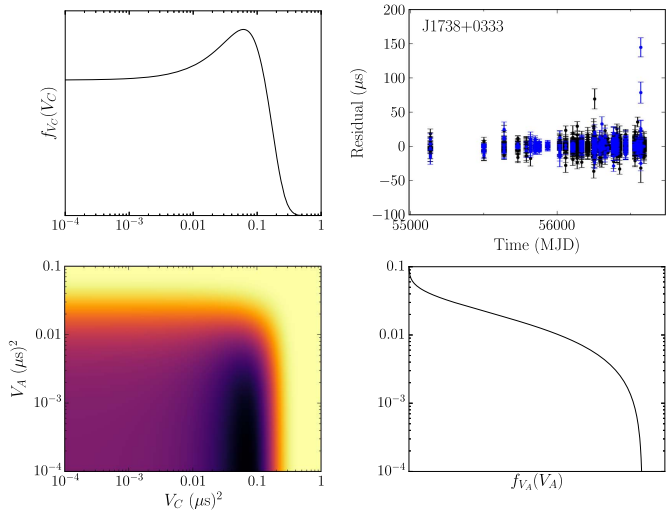

Figure 6. Achromatic/chromatic stochastic process likelihood analysis for PSR J1738+0333. See the caption to Figure 3 for more details.

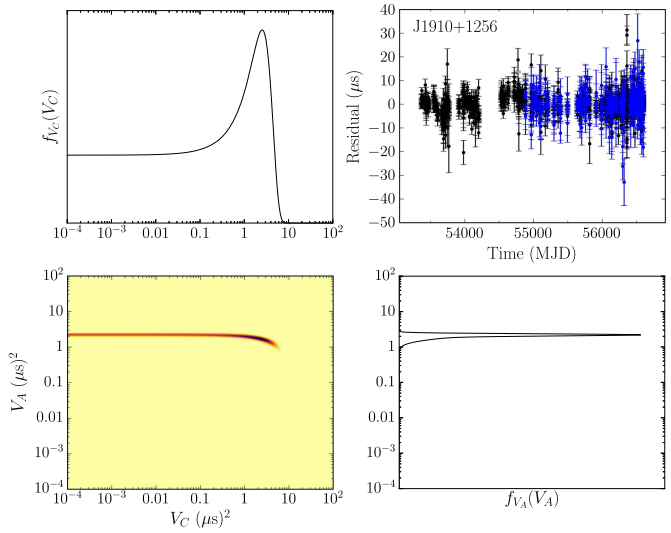

Figure 7. Achromatic/chromatic stochastic process likelihood analysis for PSR J1910+1256. See the caption to Figure 3 for more details.

sensitivity to the variance of any one in particular will be reduced. More complex noise model prescriptions may be required to successfully disentangle the variance of each. For example, a Gram–Schmidt procedure may improve the likelihood fit with an alternate parameterization (e.g., Blandford et al. 1984; Madison et al. 2013). Since we do not yet understand how to fully incorporate all interstellar propagation effects into our timing models, more work should be performed in the future that attempts to separate the variances of each process.

4.4. Comparison with the NG9 Noise Parameters

We compare our single-process excess noise measurements with the estimated noise from NG9. We choose the single-process parameterization as a more equal comparison with the previous results because chromaticity is not accounted for in NG9. Our excess noise measurements correspond to the quadratic sum of the red noise and $\mathcal{Q}$ (EQUAD).

Following the formalism in NG9, we can convert the red noise parameters $A_{\rm r}$ and $\gamma_{\rm r}$ into an rms "timing noise" after a quadratic fit of the residuals, which we can write in the form[29]

$$\sigma_{\rm TN,2} \approx \left(\int_{1/T}^{\infty} P(f)df\right)^{1/2} = 3\ \text{ns}\ (\gamma_{\rm r}-1)^{-1/2} \times \left(\frac{A_{\rm r}}{3\times10^{-3}\ \mu\text{s yr}^{1/2}}\right) T_{\rm yr}^{(\gamma_{\rm r}-1)/2}. \quad (15)$$

The result is only valid for power-law spectra when $\gamma_{\rm r} > 1$. When $\gamma_{\rm r} = 1$, the variance is proportional to $\ln(f_h T)$, where f_h is a high-frequency cutoff roughly set by the observing cadence. When $\gamma_{\rm r} < 1$, the variance is proportional to $f_h^{(1-\gamma_{\rm r})}$ and does not depend on T. The use of $1/T$ in Equation (15) as the lower-cutoff frequency is only an approximation of a filter for quadratic subtraction, the fitting for spin period and spin period derivative in the pulsar timing model. We used a more exact approach in calculating the posttiming model-fit rms that included a normalized transmission function $\mathcal{T}(f)$ derived from the spin and astrometric timing parameters that NG9 fit to all pulsars (Blandford et al. 1984). The postfit rms is therefore smaller than the value given by Equation (15). Using the formalism in Madison et al. (2013), we calculated $\mathcal{T}(f)$ and applied it to the power-law power spectra for each pulsar to numerically determine the post-fit rms from red noise as

$$\sigma_{\rm r,post} = \left(\int_{1/T}^{\infty} \mathcal{T}(f)P(f)df\right)^{1/2}. \quad (16)$$

For the WN component, since NG9 provided one value of $\mathcal{Q}$ per back-end/receiver combination, we calculated the total contribution to the excess noise from $\mathcal{Q}$ as the square root of the average quadrature value from each band weighted by the number of TOAs for each back-end/receiver combination.

Figure 11 shows the comparison between the excess noise estimated in NG9, $\sigma_{\rm ex,NG9} = [\mathcal{Q}^2 + \sigma^2_{\rm r,NG9}]^{1/2}$, and $\sigma_{\rm ex}$, where measurements in both are given by the black points, and gray points denote the cases where there is an upper limit in at least one of the two methods. We did not include $\mathcal{F}$ in the comparison because it is unclear how to relate the rescaling of the error bars in that manner to the physical quantities of the WN model we present. The inclusion of $\mathcal{F}$ in the NG9 noise estimation can bias the estimates of the other parameters. In general, our measurements are consistent with those in NG9, although with much smaller uncertainties (again because of the large covariances between the NG9 red-noise parameters); there are a few exceptions in the upper limits.

4.5. Structure Function Analysis

Up to this point, we have ignored the spectral properties of the excess noise; that is, we have not attempted to decompose the excess noise into red and white components. Residuals with red noise will have increased power at lower fluctuation frequencies in their ensemble-average power spectrum. We can use a structure function (SF) analysis to show that there is

[29] We note that Equation (15) corrects two typos in Equation (6) in NG9. The factor of "$(1-\gamma_{\rm r})$" should be "$-(1+\gamma_{\rm r})$" when the spectral index is defined oppositely as it is here, that is, $P(f) \propto f^{\gamma_{\rm r}}$. Also, the prefactor of 2.05 should be 3.0 ns.

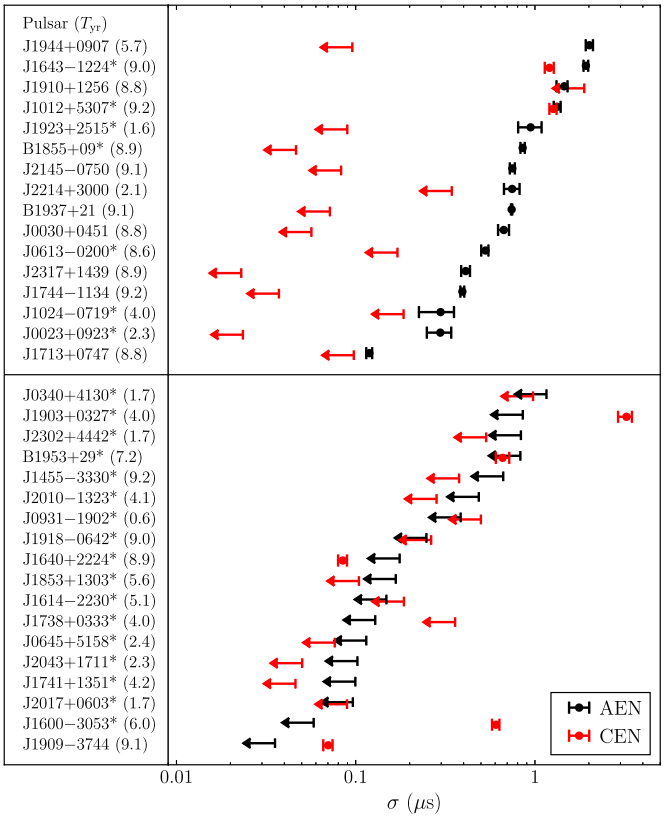

Figure 8. Measured achromatic (AEN, black) and chromatic excess noise (CEN, red) for each of the NANOGrav pulsars ranked by the achromatic noise. The numbers in parentheses are the total time span observed for each pulsar, in years. Asterisks indicate pulsars for which the white-noise model is an upper limit for at least one receiver band. Here we separate the detections of achromatic noise (top) from the upper limits (bottom).

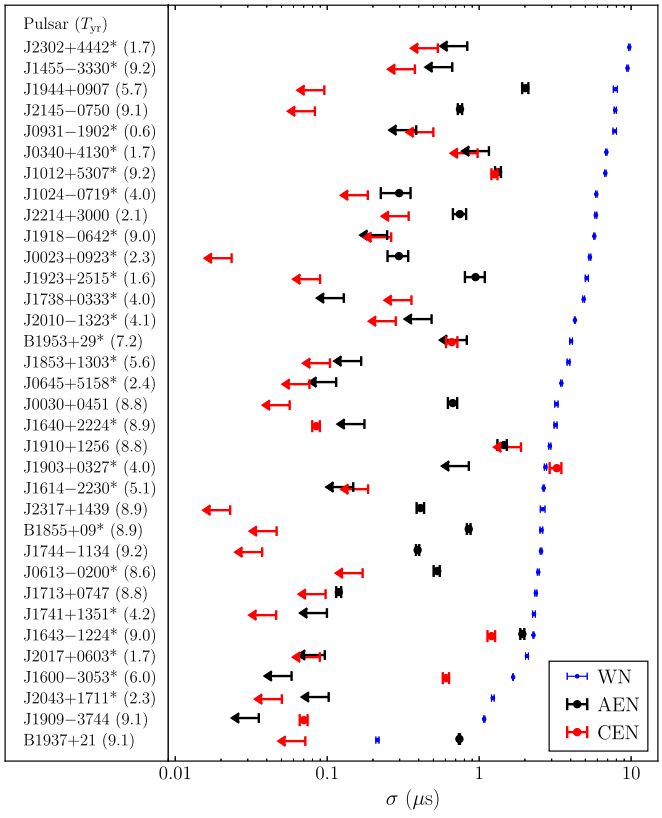

Figure 9. Measured achromatic excess noise (AEN), chromatic excess noise (CEN, red), and white noise (WN, blue, calculated as per Equation (14)) for each of the NANOGrav pulsars ranked by the white noise, showing the total noise budget for the pulsar timing array. The numbers in parentheses are the total time span observed for each pulsar, in years. Asterisks indicate pulsars for which the white noise model is an upper limit for at least one receiver band.

excess power at large time lags (low fluctuation frequencies) and demonstrate the contribution of red noise to the total excess noise budget. We expect some pulsars to be dominated by red noise upon visual inspection of the residuals, such as for PSR B1937+21. Individual pulsars with other noise properties will be discussed in the next section. An analysis of additional properties of the power spectra are outside the scope of this paper.

The SF for a time series $X(t)$ is the average squared difference/increment:

$$D_X(\tau) = \langle [X(t+\tau) - X(t)]^2 \rangle, \quad (17)$$

where τ is a time lag. It is trivial to show that for WN $W(t)$ with variance V_W, the SF is $2V_W(1 - \delta_{\tau 0})$, where δ is the Kronecker delta. Generally, the SF will be related to the variance at a given nonzero lag by a factor of 2.

Within a given epoch, we have many residuals measured at different observing frequencies that contribute large amounts of WN to the SF. Therefore, in order to reduce the influence of the WN, we computed epoch-averaged residuals as we discussed in Section 4.1. Epoch-averaging reduces the WN variance roughly by a factor of the number of residuals in an epoch (assuming equal errors), whereas the red-noise variance will remain constant.

Figures 12 and 13 show the epoch-averaged residuals (denoted as $\overline{\mathcal{R}}$) and the SFs for PSRs B1937+21 and J1713+0747, respectively. We used 20 lag bins per decade, and the maximum lag bin shown is at $\tau = 1000$ days; small-number statistics cause wild fluctuations for narrowly defined, large lag bins, so we do not show them. Errors are taken to be the rms of the increments in each lag bin. We find that many of our pulsars show increases in the SF at large ($\tau \geqslant 365$ days) lags over small ($0 < \tau \leqslant 30$ days, up to the typical cadence for each pulsar at each telescope) lags; the blue points and lines show the SF for the bins defined over the two broad ranges. We ignored contributions from the zero lag because the increments are zero, which will affect the mean of the squared increments for lags $\leqslant$30 days. Increases in the SF indicate that red noise is present in a number of the pulsars and in some cases dominates over temporally uncorrelated excess noise; for pure WN the SF values would be comparable.

To estimate the red variance, we define the redness parameter to be the ratio of the SF over the two broad lag bins:

$$\mathrm{RP} \equiv \frac{D_{\overline{\mathcal{R}}}(\tau \geqslant 365)}{D_{\overline{\mathcal{R}}}(0 < \tau \leqslant 30)} \approx \frac{2V_r + 2V_W}{2V_W} \approx \frac{V_r}{V_W} + 1. \quad (18)$$

Our redness parameter is similar in spirit to the one defined by Cordes & Downs (1985), which characterizes the redness of the power spectra using the slope of the third-order SF of the (phase) residuals. The parameter is $\mathrm{RP_{CD}} = (m_3 - 1)/2$, where m_3 is the slope of the third-order SF. The data used here are too sparse to properly estimate higher-order SFs. First-order SFs

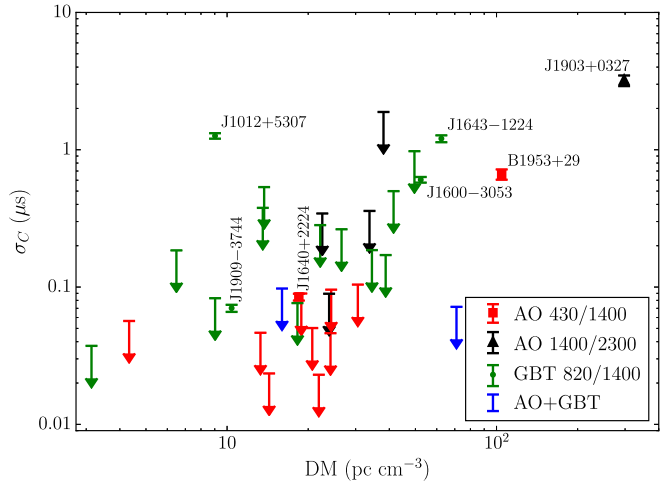

Figure 10. Chromatic excess noise (CEN) in NANOGrav pulsars versus DM. Colors denote which telescope and receiver bands were used to observe a pulsar. The two blue points represent PSRs J1713+0747 (820/1400 at GBT and 1400/2300 at AO) and B1937+21 (820/1400 at GBT and 430/1400 at AO, DM = 71.0 pc cm^{-3}).

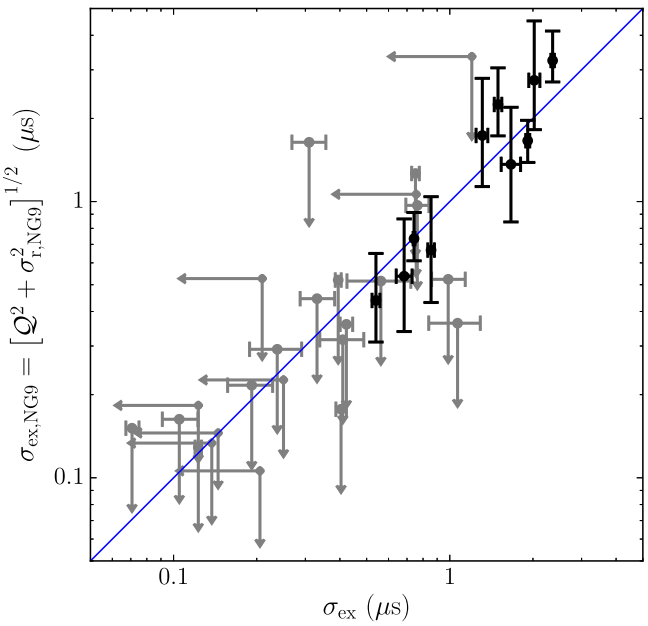

Figure 11. Comparison of excess noise between NG9 and this work. Black points denote measurements in both, and the gray points mark upper limits in at least one of the values for a given pulsar. The diagonal blue line shows where the NG9 excess noise equals $\sigma_{\rm ex}$.

like in Equation (17) scale as $\tau^{\gamma_{\rm r}-1}$ for $\gamma_{\rm r} \leqslant 3$ and saturate as τ^2 for steeper spectra; higher-order SFs allow for the characterization of steeper slopes (see, e.g., Falcon et al. 2010). Rather than impose a functional form of the power spectra in this work, we used the first-order SF to simply characterize the bulk power at low versus high fluctuation frequencies (large versus small time lags), parameterized by our form of RP.

Along with the results of the variance analyses, we show the values of RP for each pulsar in Table 3. Errors reflect the scatter of the increments in the two time-lag bins propagated from the SFs into each individual RP only; we have not accounted for realization errors (Lam et al. 2015). The

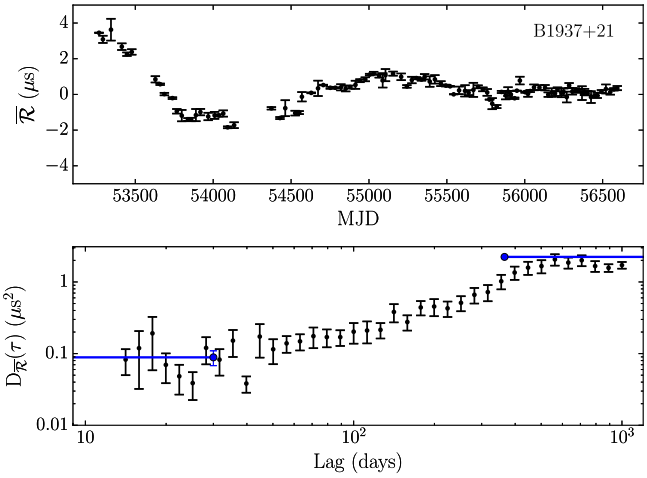

Figure 12. Epoch-averaged residuals (top) and structure function (bottom) for PSR B1937+21 with 20 lag bins per decade. The blue lines indicate the two lag-bin ranges defined as $0 < \tau \leqslant 30$ days and $\tau \geqslant 365$ days.

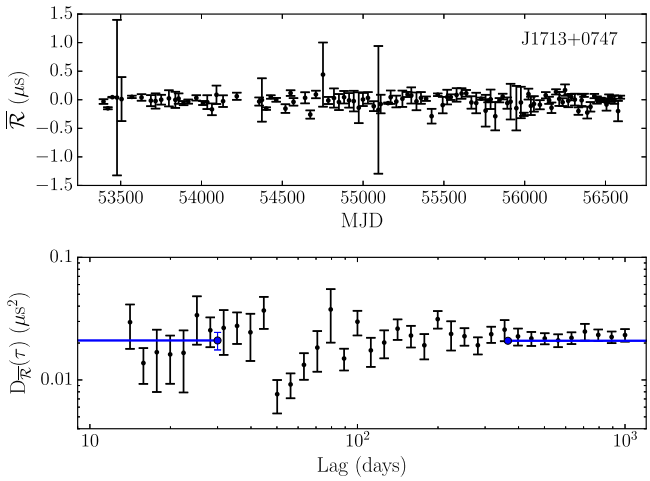

Figure 13. Epoch-averaged residuals (top) and structure function (bottom) for PSR J1713+0747 with 20 lag bins per decade. The blue lines indicate the two lag-bin ranges defined as $0 < \tau \leqslant 30$ days and $\tau \geqslant 365$ days.

uncertainties on the epoch-averaged residuals are not included and contribute nontrivially; however, any increase in the uncertainty of RP will be minimized by the large number of increments being averaged together. For convenience, we also show the fraction of the red variance versus the total variance, which is simply

$$\frac{V_r}{V_{\rm tot}} = \frac{\rm RP - 1}{\rm RP} \tag{19}$$

if we assume that the only contributions to the SF can be broken into red noise and WN components. We note that pulsars with RP values inconsistent with and less than 1 have short total observing time spans, which will cause poor estimation of the large time-lag bin. All other RP values are consistent with 1 or greater. To test for biases in our metric, we performed simulations in which we generated idealized TOAs from timing models with WN perturbations, refit the timing model to produce residuals, and then calculated the RP. When the total time span of the simulated residuals was long (∼9 yr),

we found a small (few percent) bias, but RP ≈ 1, well within the measurement errors for the real data. Thus we believe that significant departures from 1 demonstrate the presence of red noise, which we see in several of our pulsars.

Of our pulsars, 17 show significance in $V_r/V_{\rm tot}$ at the 2σ level. When combined with our 2σ criterion for the significance of an excess noise detection versus an upper limit, we find that 15 pulsars display red noise in the single-process excess noise. All pulsars with detected red noise in NG9 also show redness in our analysis.

5. INDIVIDUAL PULSAR DISCUSSION

In this section, we will describe the individual results for the NANOGrav pulsars and discuss the broader context for each. We begin with individual pulsars in name order, followed by pulsars grouped by specific characteristics at the end.

5.1. PSR J0023+0923

PSR J0023+0923 shows a detection of AEN after only $\sim$2 years of observation despite upper limits in the WN model for both receiver bands. We expect strong scintillation events to allow for future estimation of $\sigma_{\rm J}$ and therefore refinement of both the WN and AEN.

5.2. PSR J0340+4130

PSR J0340+4130 shows an upper limit in both AEN and CEN, but the log-variance likelihood for CEN shows a strong peak. With a short observed time span (1.7 years), increased observations should improve the estimate of the CEN value if the noise grows with time. Conservative errors from the upper limit on the WN, however, cause a bias in the localization of the peak. The bias will improve with better estimates of the WN. Regardless, the large value of $n_{\rm ISS}$ measured in NG9WN indicates that achieving a high enough pulse S/N via scintillation to measure $\sigma_{\rm J}$ and therefore constrain the WN parameters may be difficult in the future.

5.3. PSR J0645+5158

PSR J0645+5158 shows strong peaks in the log-variance likelihoods for both AEN and CEN after 2.4 years of observation, though we report both as upper limits based on our 2σ cutoff criterion (the single-process excess is detected). The upper limit on WN for the 1400 MHz band implies our conservative WN will remove variance from both possible red-noise processes, and therefore better estimation will yield improved localization of the peaks. The pulsar strongly scintillates, so with increased data we believe refinement of all of the noise terms should be possible in the near future.

5.4. PSR J1012+5307

PSR J1012+5307 shows strong detections of both AEN and CEN after $\sim$9 years of observation with approximately 3/4 of the excess being red. As discussed in Section 4, PSR J1012+5307 shows a large CEN compared with its DM. It does show an upper limit on the WN, so both red components will be biased. The pulsar exhibits strong scintillation events, although since it has been observed the full $\sim$9 years, we believe it will be difficult to obtain enough high-S/N pulses to determine $\sigma_{\rm J}$. There is currently no measurement of the scintillation timescale for this pulsar, indicating it is of order of typical observation timescales or longer; the NE2001 model estimates $\Delta t_{\rm d} \sim 20$ minutes at 1400 MHz (Cordes & Lazio 2002). Therefore, several long observation tracks on the pulsar may help in capturing enough bright scintles for $\sigma_{\rm J}$ determination and thus allow for faster WN parameter refinement.

5.5. PSR J1024−0719

A number of timing residuals for PSR J1024−0719 deviate significantly (many sigma) from zero and therefore contribute to the noise estimation as an excess noise beyond the WN. The values of AEN are determined to be upper limits regardless, though the true values are likely significantly lower than that reported. The cause of such discrepant residuals should be investigated in future data releases.

Additionally, Reardon et al. (2016) find that PSR J1024−0719 shows steep red noise, $P(f) \sim f^{-6}$, in disagreement with our findings, where we see significantly lower levels of red noise. The pulsar was recently shown to be in a long-period orbit (Kaplan et al. 2016; Bassa et al. 2016), where differences in the timing models for the pulsar were noted because of the unaccounted-for binary. It is possible that differences in the timing models account for the disagreement in the estimated red noise.

5.6. PSR J1455−3330

As with PSR J1024−0719, a number of timing residuals for PSR J1455−3330 deviate significantly from zero in a nonstationary way and contribute to an increase in the AEN (though an upper limit was also determined for this pulsar). The cause of the outliers is unknown and should be further investigated.

5.7. PSR J1643−1224

PSR J1643−1224 has demonstrated unusual chromatic timing behavior (Perrodin et al. 2013; Arzoumanian et al. 2015a; Lentati et al. 2016); pulse shape variations are possibly the cause (Shannon et al. 2016). It is one of four pulsars in NG9WN where $\sigma_{\rm const}$ was less than the scintillation-estimated $\sigma_{\rm DISS}$ (at 820 MHz for this pulsar). Therefore, we are unable to determine the breakdown of $\sigma_{\rm const}$ into $\sigma_{\rm J}$ and $\sigma_{\rm DISS}$ in the band. We then assumed that the entirety of $\sigma_{\rm const}$ is composed of $\sigma_{\rm J}$. NG9WN found that for most pulsars $\sigma_{\rm J} > \sigma_{\rm DISS}$, except at lower frequencies (e.g., 430 MHz), so we believe our assumption to be reasonably accurate, though with a moderately high DM of 62.4 pc cm^{-3}, DISS may play a larger role in the WN (as is true for PSR B1937+21, with DM = 71.0 pc cm^{-3}). Thus our estimates of AEN and CEN, of which a large fraction is red, will be biased high.

5.8. PSR J1713+0747

PSR J1713+0747 is considered one of the best-timed pulsars, though red noise has been measured in the pulsar previously (Splaver et al. 2005; Zhu et al. 2015; Lentati et al. 2016). The red noise was measured in Zhu et al. (2015) similarly to the method in NG9, where the power-law noise parameters were $A_{\rm r} = 0.025\ \mu{\rm s\ yr}^{1/2}$ and $\gamma_{\rm r} = -2.92$. Using Equation (15) with a time span of 8.8 years equal to the observation length in the NG9, and integrating the implied power spectrum with the appropriate transmission function $\mathcal{T}(f)$, we calculated $\sigma_{\rm r} = 120$ ns. The two-dimensional likelihood surface of $A_{\rm r}$ and $\gamma_{\rm r}$ in Zhu et al. (2015) suggests that

there can be large errors on both the amplitude and the spectral index, leading to a large fractional error on the rms red noise. Our analysis concludes that $\sigma_A = 119^{+4}_{-5}$ ns, which is consistent with the previous measurement, but we find no evidence of redness from the SF analysis.

Since PSR J1713+0747 was observed with both AO and GBT, we performed our variance analysis on the residuals from each telescope separately after we accounted for the full timing model (i.e., both telescopes used in the fit). The results are listed in Table 3. We measured 4,699 TOAs with AO and 10,530 with GBT, the significant increase corresponding to the GUPPI back end at GBT coming online before the PUPPI back end at AO. The GBT data show significantly higher excess noise as well as a detection of CEN; the chromatic noise averages into an upper limit when jointly analyzing the data. The CEN could result from the fact that the observing frequency range at GBT is lower than that at AO (1400 and 820 MHz bands versus 1400 and 2300 MHz), and therefore chromatic noise contributes more at GBT. It is interesting to note that not only is AO more sensitive, but the excess noise contribution is also less than that of GBT, though the exact cause is currently unknown.

5.9. PSR J1903+0327

PSR J1903+0327 is the pulsar with the highest DM (297.6 pc cm^{-3}) in the NANOGrav pulsar timing array and shows the largest value of CEN that is strongly red, suggesting some influence from the ISM. It shows a peak in the log-variance likelihood for AEN, although we report an upper limit based on our cutoff criterion. The large DM correlates with small scintillation bandwidths and timescales, leading to a large number of scintles across the observing band and a low probability of bright scintillation events. Therefore, estimating σ_J in the future may be difficult. Like PSR J1643−1224, NG9WN also estimated $\sigma_{\rm const}$ as less than the scintillation-estimated $\sigma_{\rm DISS}$ for PSR J1903+0327 (at 1400 MHz for this pulsar). Again, we assume that the entirety of $\sigma_{\rm const}$ is composed of jitter for consistency, though the assumption may be incorrect; the uncertainty will bias our red-noise estimates. We report a CEN measurement of $\sigma_C = 3.2^{+0.2}_{-0.3}$ μs for this pulsar, although it is observed with the 1400 and 2300 MHz receivers at AO. Scaled to the midrange frequency of ∼1800 MHz observed for this pulsar and assuming $s = 2$, we find $\sigma_{C,1800} = 1.0 \pm 0.1$ μs.

5.10. PSR J1909−3744

PSR J1909−3744 is one of the best-timed pulsars known. It shows the lowest AEN upper limit for all pulsars and was observed for the entire nine-year time span. It is the pulsar with the second-ranked total WN in NG9WN, behind PSR B1937+21, which is further confirmed in Figure 9. Due to the lack of AEN, the pulsar is the most intrinsically stable clock in the NANOGrav pulsar timing array. Since the pulsar has such high timing precision, the detected CEN may be due to frequency-dependent effects, such as misestimation from asynchronous measurements between the two receiver bands at the GBT (Lam et al. 2015). If the CEN can be mitigated in the future, it may become the overall most stable clock in our pulsar timing array.

5.11. PSR J1918−0642

As with several other pulsars, we see strong peaks in the log-variance likelihoods for both AEN and CEN (and a detection in the single-process excess). The σ_J measurement from NG9WN is an upper limit, which means that our method causes excess noise to be absorbed by the WN. The large value of $n_{\rm ISS}$ measured in the 820 MHz band implies that even after 9 years of timing, achieving a large pulse S/N to measure pulse jitter may be difficult.

5.12. PSR B1937+21

Timing residuals for PSR B1937+21 show the most obvious signature of red noise because the AEN, the vast majority of which is red from the SF analysis, dominates over the WN. This pulsar is the only one in the pulsar timing array where the AEN dominates. Sources of the achromatic red noise have been attributed to a variety of causes, including neutron star rotational irregularities (SC2010), spin perturbations from an orbiting asteroid belt (Shannon et al. 2013), and GWs. The chromatic component is thought to be due to interstellar propagation effects (Armstrong 1984; Rickett 1990; Kaspi et al. 1994; Cognard et al. 1995), such as DM and scattering variations (Cordes et al. 1990). Lentati et al. (2016) found evidence for both achromatic and chromatic noise components in the International Pulsar Timing Array Data Release 1. While the ISM has been suggested as a source of red noise, we find no evidence for any leakage of chromatic noise into the residuals for PSR B1937+21 at the ∼70 ns level (95% upper limit) over 9.1 years of timing, despite its large value of DM. However, our timing model includes a large number of $\Delta{\rm DM}_i$ bins spanning that time and the most $\Delta t_{{\rm FD},j}$ parameters (five) of any pulsar's model in our data set that can absorb CEN components.

As with PSR J1713+0747, we analyzed the residuals from each telescope independently and find that the excess noise at AO (from 2513 analyzed TOAs) is also slightly lower than that at the GBT (from 7217 analyzed TOAs). From our SF analysis, we see that the majority of the excess noise for PSR B1937+21 is red. It is unclear if the contributing red processes are common to the pulsar or the line-of-sight path, but the large majority of the variance should be from observatory-independent causes. Since both sets of residuals from each telescope derive from one global timing model fit, it is unclear how each telescope contributes to the timing model parameter estimation and therefore the postfit excess noise as well.

5.13. PSR J2010−1323

PSR J2010−1323 shows a strong peak in the log-variance likelihoods of AEN, though it does not meet our cutoff for detection, which is also likely biased from the upper limit on WN. We compute an upper limit in CEN. The pulsar weakly scintillates, and therefore it will be difficult to constrain σ_J, especially at the 820 MHz receiver band, where the number of scintles observed is large.

5.14. PSR J2017+0603

PSR J2017+0603 was observed in three different receiver bands in NG9 and shows upper limits in both red noise components. The WN parameters at 430 and 1400 MHz are not well constrained, though less than 2 years of data have been

collected. The pulsar strongly scintillates at 1400 MHz, so a measurement of σ_J should be possible in the near future. At 430 MHz, the number of scintles is large, and coupled with the low pulse S/N, estimating jitter will be difficult. Data from the 430 MHz receiver were collected for only about one-third of the observing time span and is currently no longer observed using the receiver. Therefore, refining the noise model for the receiver band is not a priority, and the data may be excluded from future timing analyses.

5.15. PSR J2317+1439

PSR J2317+1439 contains the only 327 MHz data in NG9. The pulsar was observed with both 327 MHz and 430 MHz for the majority of its total time span until the last 2 years, when 1400 MHz observations were added. We detect AEN in the timing residuals of the pulsar, and since the WN parameters were well determined for all three bands, we believe the measurement to be accurate.

5.16. Low S/N: PSRs J1747−4036, J1832−4036, J1949+3106

We excluded these pulsars from our analyses because all pulses in at least one receiver band did not meet the S/N < 3 requirement for inclusion in the NG9WN analysis (note that the time and frequency resolutions were not the same as in this work). Therefore, the WN model is undetermined for the pulsars in those specific receiver bands, and we are unable to adjust the errors on the TOAs accordingly.

5.17. Instrumental Error: PSRs J1741+1351, J1923+2515, B1953+29

We removed timing residuals between MJDs 55750 and 56020 corresponding to an instrumental error with 430 MHz data taken by the ASP receiver for these three pulsars only. PSR B1953+29 still shows chromatic excess noise, though the time span over which dual frequency data remain is only ∼1 year as compared to the total 7.2 years observed; the largely red noise may then be in part due to poor DM estimation. Similarly, only ∼1 year of dual frequency data remains for PSR J1741+1351, resulting, however, in an upper limit on CEN. PSR J1923+2515 is the pulsar observed for the shortest time span (1.6 years) that shows a detection of AEN.

5.18. Single-frequency Data with a Single DM_i Parameter: PSRs J1910+1256, J1944+0907

PSRs J1910+1256 and J1944+0907 show detections of strongly red AEN but have long spans of early single-frequency-band (1400 MHz) coverage with a much smaller frequency range using the ASP back end (for PSR J1944+0907, 430 MHz data are present for the first epoch only). A single DM was fit over a significant fraction of the total time span: 1,650 days for PSR J1910+1256, and 1,250 days for PSR J1944+0907. We therefore expect errors in the timing residuals from the time-varying DM (e.g., Lam et al. 2015), a chromatic effect. However, because the ASP bandwidth is so small, our method cannot separate chromatic noise from achromatic noise. Some large portion of the measured AEN is then actually CEN from unmodeled DM variations. Without legacy data from those time periods, those data may need to be removed from the data set for robust GW detection.

5.19. Additional Pulsars with Disagreement between σ_{const} and σ_{DISS}: PSRs J1600−3053, J1640+2224

Like PSRs J1643−1224 and J1903+0327, these two pulsars (PSR J1640+2224 at 430 MHz and PSR J1600−3053 at 820 MHz) showed a disagreement between the upper limits on σ_{const} and the scintillation-estimated σ_{DISS}. We repeated the same procedure for adjusting the WN parameters, and both show significant chromatic red noise.

5.20. AEN Detections, CEN Upper Limits: PSRs J0030+0451, J0613−0200, J1744−1134, B1855+09, J2145−0750, J2214+3000

These pulsars show detections of AEN and upper limits of CEN, four of which show a strongly red residual: PSRs J0030+0451, J0613−0200, B1855+09, and J2145−0750, with J1744−1134 showing a significant detection of red noise. PSR J2214+3000 was only observed for ∼2 years while the rest were observed for ∼9 years. PSR J0613−0200 shows an AEN detection despite an upper limit in the WN model for both receiver bands. The large number of scintles n_{ISS} implies that the lack of strong scintillation events may make refinement of the WN parameters, specifically σ_J, difficult in the future given the large quantity of data already available for the pulsar. The AEN value is therefore biased for PSR J0613−0200. Reardon et al. (2016) find steep red noise in this pulsar $P(f) \sim f^{-5}$, and our large value of RP (9.3 ± 2.4, the third highest value) shows some loose agreement. PSR J0030+0451 has the third highest value of RP $= 9.0 \pm 2.5$, which also loosely suggests some agreement with NG9 ($P(f) \sim f^{-6}$)

5.21. Noise Parameter Upper Limits: PSRs J0931−1902, J1614−2230, J1738+0333, J1853+1303, J2043+1711, J2302+4442

These pulsars show upper limits in both the excess noise and the WN parameters. In the case of PSRs J0931−1902, J2043+1711, and J2302+4442, the observed timespans are $\lesssim$2 years, with PSR J0931−1902 on the short end (0.6 year). It is therefore unsurprising that the noise parameters are ill-constrained for these pulsars.

The other three pulsars were observed for between 4 and 6 years but show no hints of excess noise. The WN parameters for the pulsars are not well constrained in at least one of the receiver bands, and therefore the conservative errors may be absorbing some of the excess noise. Even so, it is possible that some subset of the pulsars may turn out to be stable clocks on longer timescales. A large value of n_{ISS} was observed for PSR J1614−2230 in NG9WN, so it may be difficult to estimate σ_J for the 820 MHz band. On the reverse side, PSR J1738+0333 strongly scintillates, so σ_J may be estimated at 2300 MHz in the near future. PSR J1853+1303 shows strong scintillation at 1400 MHz but weaker potential for scintillation events at 430 MHz. The lower receiver band was only observed over the second half of the data span, however, so it is possible that increased observing will help improve both sets of WN parameters.

6. GLOBAL SCALING LAW MAXIMUM LIKELIHOOD ANALYSIS

Using our AEN measurements, we reexamined the spin-noise scaling relations of SC2010 across different pulsar

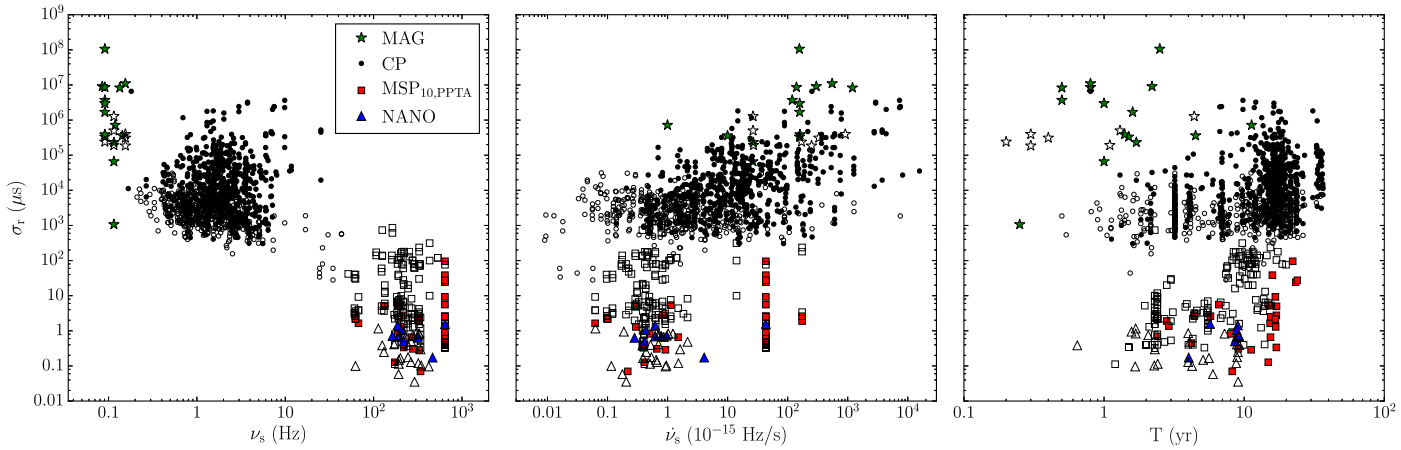

Figure 14. Measured red noise versus spin frequency (left), spin frequency derivative (middle), and observing time span (right). Green stars indicate magnetars (MAGs), black circles indicate canonical pulsars (CPs), and red squares indicate millisecond pulsars (MSPs), all from Shannon & Cordes (2010). Blue triangles indicate NANOGrav MSPs (NANO) with measurements derived from this work. Solid symbols indicate detections of red noise, while open symbols indicate upper limits.

populations: magnetars (denoted MAG), slow-period canonical pulsars (denoted CP), and MSPs. SC2010 had measured spin noise for only two MSPs (though multiple measurements per pulsar were allowed), making the NANOGrav pulsars important additions for anchoring the global fit. We estimated the amount of achromatic red noise by adjusting our AEN measurements using the RP values from Section 4.5. While the RP values characterize the total variance and not purely the achromatic noise, the process of epoch-averaging the residuals for the SF analysis reduces the chromatic noise as roughly the square root of the number of observing bands (typically two). Nevertheless, the bias is still present and introduces scatter into our measurements. We defined a red noise "detection" as when the AEN was detected and the estimate of V_r/V_{tot} was 2σ significant. Otherwise, a detection of AEN was treated as an upper limit on the achromatic red noise. For 95% upper limits on AEN, we treated those as upper limits on the red noise as well.

We also incorporated red noise results from 15 out of 20 MSPs in the Parkes Pulsar Timing Array (PPTA) extended first data release (Manchester et al. 2013). Reardon et al. (2016) modeled the achromatic red noise with a modified power law of the form

$$P(f) = \frac{P_0}{[1 + (f/f_c)^2]^{\alpha_r/2}}, \tag{20}$$

where the amplitude of the power P_0 at a corner frequency of f_c is in units of yr^3 and α_r is the spectral index. We calculated the rms red noise for each pulsar by integrating its power spectrum after applying the appropriate transmission function $\mathcal{T}(f)$ (see Equation (16)).

For our analysis, we assumed that the entirety of the achromatic red noise is due to intrinsic spin noise. Other sources of achromatic red noise, such as GWs, will bias our measurements. Excess WN from improper adjustment of the AEN will also bias our measurements. Any other pulsars for which red noise was measured in SC2010 that contain chromatic noise will also skew the results.

As in SC2010, we assumed that the red spin noise is a function of ν_s and $\dot{\nu}_s$, the pulsar spin frequency and spin frequency derivative, respectively, as well as a function of observing time span T. For all MSPs, we applied Shklovskii corrections to $\dot{\nu}_s$ where possible (Shklovskii 1970; Nice & Taylor 1995). Since the red noise σ_r was attributed to rotational spin noise alone, σ_r is entirely a function of the two basic pulsar spin observables and time. SC2010 argues that for most pulsars, spin noise is the dominant source of excess noise. Again, at the timing precision level of MSPs, it is not clear that spin noise should be the dominant term. However, while the MSP spin noise values will be biased, the global trends in overall red noise remain the same. Therefore, we believe that using the three-observable formalism with parameters that only represent spin noise is adequate to describe the red noise in general, though more parameters may be required in the future. For example, if a trend is present in Figure 10, then a scaling in DM should be included in the fit.

Figure 14 shows the red noise as a function of the three observables. The different pulsar populations are displayed with differently shaped symbols, and we explicitly separate the NANOGrav pulsars from the other MSPs provided in SC2010 and Reardon et al. (2016), denoted as $\mathrm{MSP}_{10,\mathrm{PPTA}}$. Detections of red noise are given by the solid symbols, and upper limits are given by the open ones.

Following SC2010, we write the rms red noise after a timing-model fit as

$$\hat{\sigma}_r(\nu_s, \dot{\nu}_s, T|C_2, \alpha, \beta, \gamma) = C_2 \nu_{s,\mathrm{Hz}}^{\alpha} |\dot{\nu}_{s,-15}|^{\beta} T_{yr}^{\gamma}\ \mu s \tag{21}$$

where C_2, α, β, and γ are parameters to be estimated over each pulsar included in the analysis. We include a parameter δ that accounts for the scatter in the red-noise amplitude. For detections of red noise, we assume that the variance is log-normally distributed, represented with a PDF:

$$f_D(\sigma_r|\{\nu_s, \dot{\nu}_s, T\}, \{C_2, \alpha, \beta, \gamma, \delta\}) = \frac{1}{\sqrt{2\pi\delta^2}} \times \exp\left(-\frac{[\ln \sigma_r - \ln \hat{\sigma}_r(\nu_s, \dot{\nu}_s, T|C_2, \alpha, \beta, \gamma)]^2}{2\delta^2}\right). \tag{22}$$

For upper-limit measurements on the excess noise, we use the survival function of the log-normal distribution (e.g., see Lawless 2005, p. 6 for a review, noting that an upper-limit likelihood is equivalent to a left-censored distribution, or 1 minus the survival function) to calculate the appropriate

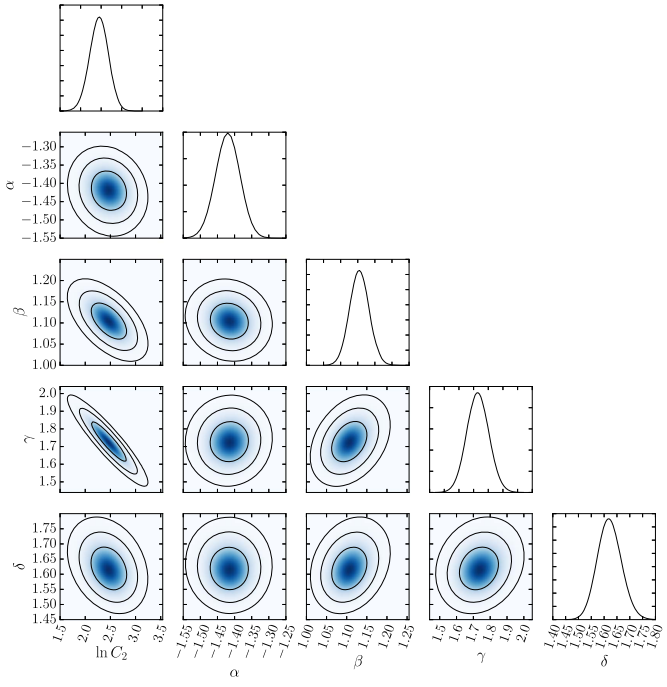

Figure 15. Global spin-noise maximum likelihood analysis results when computed for all pulsars. The colored regions show the two-dimensional marginalized distributions, with the contours encapsulating 68.3%, 95.5%, and 99.7% of the total probability. The line plots show the one-dimensional marginalized distributions from which the parameter estimates are calculated.

distribution for upper limits as

$$f_{\rm UL}\left(\sigma_{\rm r}|\{\nu_{\rm s},\,\dot{\nu}_{\rm s},\,T\},\,\{C_2,\,\alpha,\,\beta,\,\gamma,\,\delta\}\right) = \frac{1}{2}\left(1+\mathrm{erf}\left[\frac{\ln\sigma_{\rm r}-\ln\hat{\sigma}_{\rm r}(\nu_{\rm s},\,\dot{\nu}_{\rm s},\,T|C_2,\,\alpha,\,\beta,\,\gamma)}{\delta\sqrt{2}}\right]\right), \quad (23)$$

where erf is the error function. We note that the order of the argument to erf presented here corrects a typo in SC2010, which is reversed by a negative sign.

We define our five-parameter likelihood function as

$$\mathcal{L}(C_2,\,\alpha,\,\beta,\,\gamma,\,\delta|\{\sigma_{{\rm r},i},\,\nu_{{\rm s},i},\,\dot{\nu}_{{\rm s},i},\,T_i\}) = \prod_j f_{\rm D}\left(\sigma_{{\rm r},j}|\{\nu_{{\rm s},j},\,\dot{\nu}_{{\rm s},j},\,T_j\},\,\{C_2,\,\alpha,\,\beta,\,\gamma,\,\delta\}\right) \times \prod_k f_{\rm UL}\left(\sigma_{{\rm r},k}|\{\nu_{{\rm s},k},\,\dot{\nu}_{{\rm s},k},\,T_k\},\,\{C_2,\,\alpha,\,\beta,\,\gamma,\,\delta\}\right) \quad (24)$$

where i labels all of the individual measurements, j labels the subset of measurements with detected red noise, and k labels the subset of measurements with upper limits on the red noise. We performed a linear grid search over the five parameters $\ln C_2$, α, β, γ, δ with a range and resolution to sufficiently sample the parameter space. For computational stability, we first computed the log-likelihood as the sum of the log-PDFs in Equation (24).

Figure 15 shows the likelihood analysis run with all pulsars included. Parameters were estimated by taking the one-dimensional marginalized distributions, computing the cumulative distribution function, and finding the $\pm 34.1\%$ confidence regions about the maximum likelihood value. We performed a similar analysis over different subsets of the pulsar populations and provide our results in Table 4.

Figure 16 shows the measured red noise versus the model red noise using the maximum likelihood model parameters when computed for all pulsars. The addition of the NANOGrav and PPTA pulsars to the fit helps constrain the power-law relations at lower $\nu_{\rm s}$ and $\dot{\nu}_{\rm s}$ as compared with SC2010, which only contained (multiple estimates of) detected noise in two MSPs. We note that the global fit tends to underestimate the spin noise in the NANOGrav pulsars slightly as compared with the total MSP population; the cause could be from the differences in timing models between NANOGrav and other measurements, but it is unclear from the values alone. In addition, the values for magnetars are also underestimated, suggesting either that systematic bias is present when trying to fit over all pulsar populations or that the different pulsar populations are not fit by a single scaling law.

For the NANOGrav-only data (NANO), we find that our three scaling parameters $\{\alpha,\,\beta,\,\gamma\}$ are all roughly consistent with zero, reflecting that the red-noise measurements by themselves are generally unconstraining. In terms of the scaling with time γ, we also suffer from the fact that most of our detections of red noise are in pulsars that have been observed for $\sim$9 years, making constraints on γ difficult. For the combined $\mathrm{MSP}_{10,\mathrm{PPTA}}$ and NANO model, we see a steeper dependence with time than for the global fit. The largest values of $\sigma_{\rm r}$ (detections $\gtrsim 10\ \mu$s), with the largest T, are entirely from PSR B1937+21, suggesting that this pulsar alone is driving the steep fit. How representative the pulsar is of the MSP population is currently unclear (see Section 5.12).

7. CONCLUSIONS

We examined the amount of posttiming model-fit excess noise in NANOGrav timing residuals beyond the measured WN. After reweighting our TOAs, we detected excess noise in 26 of our pulsars. Splitting the excess noise into achromatic and chromatic components, as well as determining the redness of the power spectra of the residuals for each pulsar, will help us in attributing the proper amount of noise to different physical sources. Using the achromatic red-noise estimates, we were then able to further bound the global pulsar scaling relations for spin noise. While chromatic noise is possibly correctable, as well as any achromatic WN, it is unclear if that is true for the achromatic red noise, and by how much.

The addition of measurements from the NANOGrav pulsars helps constrain the spin-noise scaling relations first derived in SC2010 by anchoring the fit at lower $\nu_{\rm s}$ and $\dot{\nu}_{\rm s}$. The global scaling relation derived from using all of the pulsars will be minimally affected by uncertainties in our red-noise estimates, due to the many orders of magnitude spanned in the parameters for all of the pulsars. For a process with a power spectrum $P(f) \propto f^{-\gamma_{\rm r}}$, the spectral index $\gamma_{\rm r}$ is related to the spin-noise scaling parameter γ by $\gamma_{\rm r} = 2\gamma + 1$ (Arzoumanian et al. 2015b). Therefore, for $\gamma = 1.73 \pm 0.08$ from the fit over all pulsar populations, the noise in residuals described with a power-law spectrum will have a spectral index of $\gamma_{\rm red} = 4.46 \pm 0.16$. It is not clear from our analysis if such a scaling law applies to individual pulsar populations, and while the MSP-only fit (both $\mathrm{MSP}_{10,\mathrm{PPTA}}$ and NANO) suggests even larger values of spin noise in time, it is possible that PSR B1937+21 alone is dominating our fit, potentially biasing the population parameter estimate. However, we expect GWs to contribute to our red-noise estimates, so it is likely that some component of our achromatic noise is due to GWs; a

Table 4
Best-fit Excess Noise Parameters

Fit	$\ln C^2$	α	β	γ	δ	$N_D(N_{UL})$[a]
CP	2.1 ± 0.3	-0.85 ± 0.09	0.99 ± 0.03	1.86 ± 0.09	1.54 ± 0.05	575(458)
MAG	$0.4^{+5.4}_{-5.6}$	$-2.7^{+2.4}_{-2.5}$	1.4 ± 0.4	$2.4^{+0.7}_{-0.6}$	$1.9^{+0.5}_{-0.4}$	15(7)
$MSP_{10,PPTA}$	0.7 ± 2.7	-1.2 ± 0.5	0.8 ± 0.1	2.2 ± 0.3	1.0 ± 0.1	27(147)
NANO	-16^{+14}_{-17}	$0.8^{+2.2}_{-2.0}$	$0.9^{+0.7}_{-0.6}$	$4.9^{+4.9}_{-2.6}$	$1.7^{+1.2}_{-0.7}$	9(25)
CP+MAG	2.5 ± 0.3	-1.35 ± 0.08	1.11 ± 0.04	1.67 ± 0.08	1.64 ± 0.05	590(465)
CP+$MSP_{10,PPTA}$	1.8 ± 0.3	-1.31 ± 0.04	1.08 ± 0.03	1.95 ± 0.08	1.56 ± 0.05	602(605)
$MSP_{10,PPTA}$+NANO	-1.2 ± 2.5	-0.9 ± 0.4	0.8 ± 0.1	$2.3^{+0.3}_{-0.2}$	1.1 ± 0.1	36(172)
CP+$MSP_{10,PPTA}$+NANO	$1.8^{+0.2}_{-0.3}$	-1.32 ± 0.04	1.08 ± 0.03	1.96 ± 0.08	1.56 ± 0.05	611(630)
CP+MAG+$MSP_{10,PPTA}$	2.5 ± 0.2	-1.43 ± 0.04	1.11 ± 0.03	1.73 ± 0.08	1.62 ± 0.05	617(612)
CP+MAG+$MSP_{10,PPTA}$+NANO	2.5 ± 0.2	-1.42 ± 0.04	1.10 ± 0.03	1.73 ± 0.08	1.62 ± 0.05	626(637)

Notes. The model used for discussion in the text and subsequent figures is the final one, which includes all pulsars in the fit.
[a] The N_D values are the number of detected measurements of excess noise, while N_{UL} are the number of upper-limit measurements.

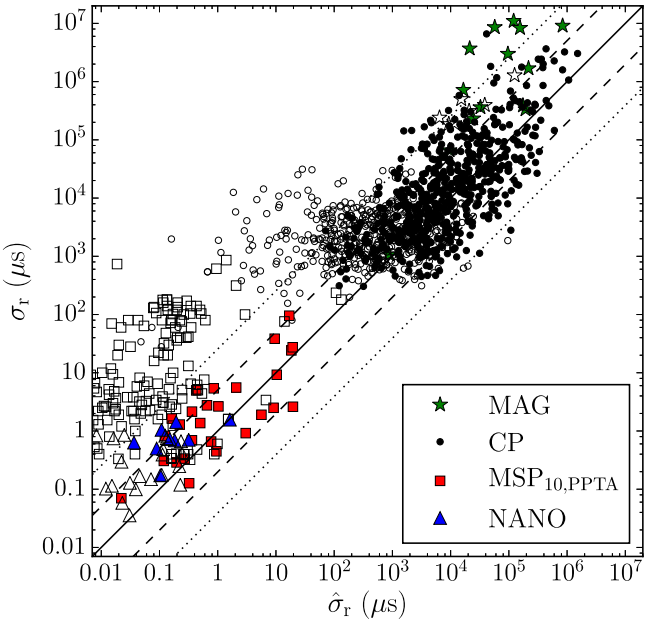

Figure 16. Measured excess noise vs. model excess noise from Equation (21) and using global parameters fit over all pulsars as given in Table 4. Symbols are as defined in Figure 14, with solid symbols being detections and open symbols being upper limits. The solid line shows where the measured excess noise equals the model excess noise, and the dashed and dotted lines show the 1σ and 2σ errors as estimated by δ, respectively.

power-law GW background will cause timing residuals with a $\gamma_r = 13/3$ spectrum, although recent work finds evidence for a deficit of power at low fluctuation frequencies (Arzoumanian et al. 2016). Understanding how the different sources of red noise in MSPs scale with time is crucial for time-to-detection estimates for GWs and for understanding long-term usability of MSPs in a pulsar timing array. Improved estimation of the red noise in the future, either with new measurements or with refinements of the current measurements (e.g., the decomposition into red and white), is of vital importance.

As demonstrated by the Laser Interferometer Gravitational-Wave Observatory's recent detection of GWs, understanding the noise within the detector is imperative for the instrument's capability to detect GWs (Abbott et al. 2016a, 2016b). With NANOGrav and other collaborations moving toward the detection of low-frequency GWs, we require full noise characterization of our pulsar timing arrays. Implementation of the full noise model we describe will help remove biases on timing parameter estimation and improve sensitivity toward the growing GW signal in our data.

We thank Paul Baker for the useful discussion regarding the methods. The NANOGrav Project receives support from NSF PIRE program award number 0968296 and NSF Physics Frontier Center award number 1430284. NANOGrav research at UBC is supported by an NSERC Discovery Grant and Discovery Accelerator Supplement and the Canadian Institute for Advanced Research. M.T.L. acknowledges partial support by NASA New York Space Grant award number NNX15AK07H. J.A.E. acknowledges support by NASA through Einstein Fellowship grant PF3-140116. Portions of this research were carried out at the Jet Propulsion Laboratory, California Institute of Technology, under a contract with the National Aeronautics and Space Administration. T.T.P. was a student at the National Radio Astronomy Observatory (NRAO) while this project was undertaken. Data for the project were collected using the facilities of the NRAO and the Arecibo Observatory. The NRAO is a facility of the NSF operated under cooperative agreement by Associated Universities, Inc. The Arecibo Observatory is operated by SRI International under a cooperative agreement with the NSF (AST-1100968), and in alliance with the Ana G. Méndez-Universidad Metropolitana, and the Universities Space Research Association.

AUTHOR CONTRIBUTIONS

M.T.L. developed the mathematical framework, created the modified data set and residuals, undertook the analysis, and prepared the majority of the text, figures, and tables. J.M.C. and S.C. helped with the development of the framework, the format of figures and tables, and generated some additional text. R.M.S. provided useful guidance with the data and interpretation of results in SC2010. J.A.E. developed the noise model in NG9 and assisted in comparison with the previous noise-analysis results, as well as provided a forum for discussion of NANOGrav's noise budget along with D.R.M. and X.S. Z.A., K.C., P.B.D., T.D., J.A.E., R.D.F., E.F., M.E.G., G.J., M.J., M.T.L., L.L., M.A.M., D.J.N., T.T.P., S.M.R., I.H.S., K.S., J.K.S., and W.W.Z. all ran observations and developed timing models for the NG9 data set. Additional specific contributions are described in Arzoumanian et al. (2015b).

REFERENCES

Abbott, B. P., Abbott, R., Abbott, T. D., et al. 2016a, PhRvL, 116, 061102
Abbott, B. P., Abbott, R., Abbott, T. D., et al. 2016b, CQGra, 33, 134001
Armstrong, J. W. 1984, Natur, 307, 527
Arzoumanian, Z., Brazier, A., Burke-Spolaor, S., et al. 2014, ApJ, 794, 141
Arzoumanian, Z., Brazier, A., Burke-Spolaor, S., et al. 2015a, ApJ, 810, 150
Arzoumanian, Z., Brazier, A., Burke-Spolaor, S., et al. 2015b, ApJ, 813, 65
Arzoumanian, Z., Brazier, A., Burke-Spolaor, S., et al. 2016, ApJ, 821, 13
Bassa, C. G., Janssen, G. H., Stappers, B. W., et al. 2016, MNRAS, 460, 2207
Blandford, R., Romani, R. W., & Narayan, R. 1984, JApA, 5, 369
Cognard, I., Bourgois, G., Lestrade, J.-F., et al. 1995, A&A, 296, 169
Coles, W., Hobbs, G., Champion, D. J., Manchester, R. N., & Verbiest, J. P. W. 2011, MNRAS, 418, 561
Cordes, J. M., & Downs, G. S. 1985, ApJS, 59, 343
Cordes, J. M., & Lazio, T. J. W. 2002, arXiv:astro-ph/0207156
Cordes, J. M., & Rickett, B. J. 1998, ApJ, 507, 846
Cordes, J. M., & Shannon, R. M. 2010, arXiv:1010.3785
Cordes, J. M., Shannon, R. M., & Stinebring, D. R. 2016, ApJ, 817, 16
Cordes, J. M., Wolszczan, A., Dewey, R. J., Blaskiewicz, M., & Stinebring, D. R. 1990, ApJ, 349, 245
Craft, H. D., Jr. 1970, PhD thesis, Cornell Univ.
Demorest, P. B. 2007, PhD thesis, Univ. California
Demorest, P. B., Ferdman, R. D., Gonzalez, M. E., et al. 2013, ApJ, 762, 94
Detweiler, S. 1979, ApJ, 234, 1100
DuPlain, R., Ransom, S., Demorest, P., et al. 2008, Proc. SPIE, 7019, 70191D
Falcon, E., Roux, S. G., & Audit, B. 2010, EL, 90, 50007
Ford, J. M., Demorest, P., & Ransom, S. 2010, Proc. SPIE, 7740, 77400A
Foster, R. S., & Backer, D. C. 1990, ApJ, 361, 300
Foster, R. S., & Cordes, J. M. 1990, ApJ, 364, 123
Hellings, R. W., & Downs, G. S. 1983, ApJL, 265, L39
Hobbs, G. B., Edwards, R. T., & Manchester, R. N. 2006, MNRAS, 369, 655
Hotan, A. W., van Straten, W., & Manchester, R. N. 2004, PASA, 21, 302
Kaplan, D. L., Kupfer, T., Nice, D. J., et al. 2016, ApJ, 826, 86
Kaspi, V. M., Taylor, J. H., & Ryba, M. F. 1994, ApJ, 428, 713
Keith, M. J., Coles, W., Shannon, R. M., et al. 2013, MNRAS, 429, 2161
Lam, M. T., Cordes, J. M., Chatterjee, S., et al. 2016a, ApJ, 819, 155
Lam, M. T., Cordes, J. M., Chatterjee, S., et al. 2016b, ApJ, 821, 66
Lam, M. T., Cordes, J. M., Chatterjee, S., & Dolch, T. 2015, ApJ, 801, 130
Lawless, J. F. 2005, Encycl. Biostat., 6
Lentati, L., Shannon, R. M., Coles, W. A., et al. 2016, MNRAS, 458, 2161
Levin, L., McLaughlin, M. A., Jones, G., et al. 2016, ApJ, 818, 166
Madison, D. R., Chatterjee, S., & Cordes, J. M. 2013, ApJ, 777, 104
Manchester, R. N., Hobbs, G., Bailes, M., et al. 2013, PASA, 30, e017
McLaughlin, M. A. 2013, CQGra, 30, 224008
Nice, D. J., & Taylor, J. H. 1995, ApJ, 441, 429
Pennucci, T. T., Demorest, P. B., & Ransom, S. M. 2014, ApJ, 790, 93
Perrodin, D., Jenet, F., Lommen, A., et al. 2013, arXiv:1311.3693
Reardon, D. J., Hobbs, G., Coles, W., et al. 2016, MNRAS, 455, 1751
Rickett, B. J. 1990, ARA&A, 28, 561
Romani, R. W. 1989, in Proc. NATO Advanced Science Institutes (ASI) Series C, Vol. 262, Timing Neutron Stars, ed. H. Ögelman & E. P. J. van den Heuvel (Dordrecht: Kluwer), 113
Sazhin, M. V. 1978, SvA, 22, 36
Shannon, R. M., & Cordes, J. M. 2010, ApJ, 725, 1607
Shannon, R. M., Cordes, J. M., Metcalfe, T. S., et al. 2013, ApJ, 766, 5
Shannon, R. M., Lentati, L. T., Kerr, M., et al. 2016, ApJL, 828, L1
Shannon, R. M., Osłowski, S., Dai, S., et al. 2014, MNRAS, 443, 1463
Shklovskii, I. S. 1970, SvA, 13, 562
Splaver, E. M., Nice, D. J., Stairs, I. H., Lommen, A. N., & Backer, D. C. 2005, ApJ, 620, 405
Taylor, J. H. 1992, RSPTA, 341, 117
Tiburzi, C., Hobbs, G., Kerr, M., et al. 2016, MNRAS, 455, 4339
van Straten, W. 2013, ApJS, 204, 13
van Straten, W., Demorest, P., & Osłowski, S. 2012, AR&T, 9, 237
Verbiest, J. P. W., Bailes, M., Coles, W. A., et al. 2009, MNRAS, 400, 951
Verbiest, J. P. W., Lentati, L., Hobbs, G., et al. 2016, MNRAS, 458, 1267
Will, C. M. 2014, LRR, 17, 4
Zhu, W. W., Stairs, I. H., Demorest, P. B., et al. 2015, ApJ, 809, 41